Massive binary black holes from Population II and III stars

Massive binary black holes from Population II and III stars

Guglielmo Costa[1,2,3,4] ★, Michela Mapelli[1,2,3,5] †, Giuliano Iorio[1,2,3] ‡, Filippo Santoliquido[1,2], Gastón J. Escobar[1,2], Ralf S. Klessen[5], and Alessandro Bressan[6,3]

[1]*Dipartimento di Fisica e Astronomia Galileo Galilei, Università di Padova, Vicolo dell'Osservatorio 3, I–35122 Padova, Italy*
[2]*INFN-Padova, Via Marzolo 8, I–35131 Padova, Italy*
[3]*INAF-Padova, Vicolo dell'Osservatorio 5, I–35122 Padova, Italy*
[4]*Univ Lyon, Univ Lyon1, Ens de Lyon, CNRS, Centre de Recherche Astrophysique de Lyon UMR5574, F-69230 Saint-Genis-Laval, France*
[5]*Universität Heidelberg, Zentrum für Astronomie, Institut für Theoretische Astrophysik, Albert-Ueberle-Str. 2, D–69120 Heidelberg, Germany*
[6]*SISSA, via Bonomea 365, I–34136 Trieste, Italy*

Accepted XXX. Received YYY; in original form ZZZ

ABSTRACT

Population III stars, born from the primordial gas in the Universe, lose a negligible fraction of their mass via stellar winds and possibly follow a top-heavy mass function. Hence, they have often been regarded as the ideal progenitors of massive black holes (BHs), even above the pair instability mass gap. Here, we evolve a large set of Population III binary stars (metallicity $Z = 10^{-11}$) with our population-synthesis code SEVN, and compare them with Population II binary stars ($Z = 10^{-4}$). In our models, the lower edge of the pair-instability mass gap corresponds to a BH mass of ≈ 86 (≈ 91) $M_\odot$ for single Population III (II) stars. Overall, we find only mild differences between the properties of binary BHs (BBHs) born from Population III and II stars, especially if we adopt the same initial mass function and initial orbital properties. Most BBH mergers born from Population III and II stars have primary BH mass below the pair-instability gap, and the maximum secondary BH mass is < 50 $M_\odot$. Only up to $\approx 3.3\%$ ($\approx 0.09\%$) BBH mergers from Population III (II) progenitors have primary mass above the gap. Unlike metal-rich binary stars, the main formation channel of BBH mergers from Population III and II stars involves only stable mass transfer episodes in our fiducial model.

Key words: black hole physics – stars: Population II – stars: Population III – gravitational waves – methods: numerical

1 INTRODUCTION

Population III (hereafter, Pop. III) stars formed from metal-free primordial gas in the early Universe, and have eluded any attempt to observe them to date (e.g., Bromm & Larson 2004; Klessen & Glover 2023, for a review). Their initial mass function (IMF) is commonly considered to be more top-heavy than that of metal-rich stars, mostly because molecular hydrogen is an inefficient coolant with respect to dust (e.g., Bromm & Larson 2004; Schneider et al. 2006; Stacy & Bromm 2013; Susa et al. 2014; Hirano et al. 2014, 2015; Wollenberg et al. 2020; Chon et al. 2021; Tanikawa et al. 2021b; Jaura et al. 2022; Prole et al. 2022; Park et al. 2023). Massive Pop. III stars lose a negligible fraction of their mass during their life, because stellar winds are highly inefficient for a nearly metal-free chemical composition (e.g., Woosley et al. 2002; Volpato et al. 2023). If Pop. III stars avoid pair instability (Woosley 2017), they might thus end their life with a direct collapse, leading to the formation of massive black holes (BHs, e.g., Woosley et al. 2002). For this reason, Pop. III stars have been extensively studied (e.g., Kinugawa et al. 2014; Belczynski et al. 2017; Kinugawa et al. 2020; Tanikawa et al. 2021b, 2022a) as possible progenitors of the most massive BHs observed by the LIGO–Virgo–KAGRA (LVK) collaboration (Abbott et al. 2020a,b, 2021a,b).

Population II (hereafter, Pop. II) stars formed from material that was already enriched in metals by Pop. III stars. With a metallicity[1] ranging from $Z \sim 10^{-6}$ to a few $\times 10^{-4}$ Pop. II stars are way more common in the Universe than Pop. III stars (e.g., Smith et al. 2015): we observe them in metal-poor globular clusters, as well as in the halo of the Milky Way and in some metal-poor dwarf galaxies (e.g., Frebel et al. 2007; Frebel & Norris 2015). It is still unclear whether Pop. II stars follow the same IMF as metal-rich stars (e.g., Schneider et al. 2012; Chiaki et al. 2018; Chon et al. 2021; Sharda & Krumholz 2022). Their metal content is still sufficiently low that stellar winds are heavily quenched in Pop. II stars, too (e.g., Chen et al. 2015). Thus, massive Pop. II stars might also collapse leaving massive compact remnants at the end of their life, but their contribution to the population of BHs and intermediate-mass BHs has been less investigated than that of Pop. III stars (Spera & Mapelli 2017; Renzo et al. 2020a).

Both massive Pop. III and Pop. II stars are expected to undergo pair instability or pulsational pair instability if their central temperature and density lead to an efficient production of electron and positron pairs (Fowler & Hoyle 1964; Barkat et al. 1967; Rakavy & Shaviv

★ E-mail: guglielmo.costa.astro@gmail.com
† E-mail:michela.mapelli@unipd.it
‡ E-mail: giuliano.iorio.astro@gmail.com

[1] Here and in the following, we define Z as the mass fraction of elements heavier than helium, in absolute values.

1967; Woosley et al. 2007). If the helium core mass grows to $\sim 64 - 135\ M_\odot$ at the end of carbon burning, the star is expected to be completely disrupted by a pair instability supernova, leaving no compact remnant, while higher He-core masses enable the direct collapse of the star to a BH (Woosley et al. 2002). For He-core masses in the range $\sim 32 - 64\ M_\odot$ (Woosley 2017, 2019; Marchant et al. 2019; Farmer et al. 2019), pair instability triggers pulsations of the star, which enhance mass loss and, in the end, allow the star to find a stable configuration. While the boundaries of pair instability and the final compact remnant masses are still highly uncertain (e.g., Leung et al. 2019; Farmer et al. 2019, 2020; Marchant et al. 2019; Stevenson et al. 2019; Renzo et al. 2020a; Marchant et al. 2021; Mapelli et al. 2020; Costa et al. 2021; Woosley & Heger 2021; Vink et al. 2021), this process has a key impact on the final population of binary BHs (BBHs) born from metal-free and metal-poor stars.

Here, we model a population of BHs and BBHs born from Pop. III and Pop. II stars. Our Pop. III (II) star models assume a metallicity $Z = 10^{-11}$ ($Z = 10^{-4}$). We probe a large range of initial configurations for the IMF and orbital parameters of Pop. III and II binary stars. We show that the differences between the two BH populations are subtle. Both Pop. II and III stars can give birth to very massive BHs above the pair instability mass gap. However, most BBH mergers born via isolated binary evolution host BHs below the pair-instability mass gap. When the initial semi-major axis distribution is skewed toward small values ($< 10^3\ R_\odot$), the vast majority of BBH mergers originate from Pop. III and Pop. II binary stars that evolve only via stable mass transfer, without common envelope. In a companion paper (Santoliquido et al. 2023), we explore the impact of these models on the cosmic merger rate of BBHs.

This paper is structured as follows. In Section 2 we describe our stellar tracks and population synthesis simulations. Section 3 summarizes our main results, that we discuss in Section 4 by considering the main formation channels of the simulated BBH mergers. We draw our main conclusions in Section 5.

2 METHODS

2.1 Binary population synthesis code (SEVN)

In this work, we use the SEVN code version 2 (Iorio et al. 2023). SEVN integrates the evolution of stellar properties (e.g., total mass, photospheric radius, luminosity, helium and carbon-oxygen core mass and radius) by interpolating a set of stellar tracks (Spera & Mapelli 2017), and models the main binary evolution processes (mass transfer via stellar winds, Roche lobe overflow, common envelope evolution, tides, and gravitational-wave decay) according to the semi-analytic formalism presented in Hurley et al. (2002), with several updates described in Iorio et al. (2023). In the following, we adopt the same set up as the fiducial model presented in Iorio et al. (2023). In particular, Roche-lobe overflow mass transfer is always stable for main sequence (MS) and Hertzsprung gap donor stars, while we follow the prescriptions by Hurley et al. (2002) in all the other cases. We model the mass accretion rate during Roche-lobe overflow as

$$\dot{M}_{\rm a} = \begin{cases} \min\left(\dot{M}_{\rm Edd},\ -f_{\rm MT}\,\dot{M}_{\rm d}\right) & \text{if the accretor is a compact object,} \\ -f_{\rm MT}\,\dot{M}_{\rm d} & \text{otherwise,} \end{cases} \tag{1}$$

where $\dot{M}_{\rm Edd}$ is the Eddington rate (Eq. 67 of Hurley et al. 2002), $\dot{M}_{\rm d}$ is the mass-loss rate of the donor star, and $f_{\rm MT} \in [0, 1]$ is the mass accretion efficiency; here, we use $f_{\rm MT} = 0.5$. Furthermore, we assume that the mass not accreted during the Roche-lobe overflow is lost from the vicinity of the accretor as an isotropic wind (isotropic re-emission). At the onset of Roche-lobe overflow, SEVN circularises the orbit at periastron.

To model a common-envelope phase, we assume an efficiency parameter $\alpha_{\rm CE} = 1$ and estimate the envelope binding energy using the same $\lambda_{\rm CE}$ formalism as in Claeys et al. (2014).

We model the final fate of intermediate-mass and high-mass stars as described in Iorio et al. (2023). In particular, we use the rapid formalism by Fryer et al. (2012) for core-collapse supernovae, we model electron-capture supernovae as in Giacobbo & Mapelli (2019), and (pulsational) pair-instability supernovae according to Mapelli et al. (2020). Compact objects receive a natal kick at their birth. In our models, we randomly draw the natal kick magnitude as (Giacobbo & Mapelli 2020):

$$V_{\rm kick} = f_{\rm H05}\,\frac{\langle M_{\rm NS}\rangle}{M_{\rm rem}}\,\frac{M_{\rm ej}}{\langle M_{\rm ej}\rangle}, \tag{2}$$

where $\langle M_{\rm NS}\rangle$ and $\langle M_{\rm ej}\rangle$ are the average neutron star mass and ejecta mass from single stellar evolution, respectively, while $M_{\rm rem}$ and $M_{\rm ej}$ are the compact object mass and the ejecta mass (Giacobbo & Mapelli 2020). The term $f_{\rm H05}$ is a random number drawn from a Maxwellian distribution with one-dimensional root mean square $\sigma_{\rm kick} = 265\ {\rm km\,s^{-1}}$, coming from a fit to the proper motions of 73 young pulsars (< 3 Myr) in the Milky Way (Hobbs et al. 2005). In this formalism, stripped and ultra-stripped supernovae result in lower kicks with respect to the other explosions, owing to the lower amount of ejected mass $M_{\rm ej}$ (Bray & Eldridge 2016, 2018). BHs originating from a direct collapse receive zero natal kicks from this mechanism. We report the SEVN input parameter list in Zenodo at `https://doi.org/10.5281/zenodo.7736309` (Costa et al. 2023).

2.2 Tracks and single star evolution

We generated sets of Pop. III and Pop. II stellar tracks with the PARSEC code (Bressan et al. 2012; Costa et al. 2021, 2022; Nguyen et al. 2022). Pop. III stars have typical behaviours, which Pop. II stars do not show in their evolution (Cassisi & Castellani 1993; Marigo et al. 2001; Murphy et al. 2021). For instance, during the early MS, Pop. III stars cannot ignite the CNO tri-cycle because of the initial lack of carbon, nitrogen and oxygen. Pop. III stars need very high central temperatures to reach pressure support just with the energy provided by the proton-proton (pp) chain. Depending on the stellar mass, the central temperature becomes so high that some carbon could be synthesized from the triple-α reaction (i.e., helium burning), even in the MS. This leads the CNO tri-cycle to ignite and suddenly replace the pp chain as the main source of energy of the star (Marigo et al. 2001; Murphy et al. 2021). Moreover, due to the high central temperatures reached at the end of the MS, Pop. III stars have a smoother transition to the core helium burning (CHeB) phase with respect to more metal-rich stars. These characteristic features of Pop. III stars evolution arise at metallicity $Z \lesssim 10^{-10}$ (Cassisi & Castellani 1993). Hence, here we assume a metallicity $Z = 10^{-11}$ for Pop. III stars (see also Tanikawa et al. 2021b). For Pop. II stars, we take a metallicity $Z = 10^{-4}$.

We adopt the Caffau et al. (2011) solar partition of chemical elements. Each set has an initial mass at the zero-age main sequence (ZAMS), $M_{\rm ZAMS}$, which ranges from 2 to 600 $M_\odot$. All tracks evolve until advanced evolutionary phases. Stars with $2 \leq M_{\rm ZAMS}/M_\odot < 10$ reach the early-asymptotic giant branch (AGB) phase (post-core helium-burning phase characterized by the burning of helium in a shell above the CO core). Stars with $M_{\rm ZAMS} \geq 10\,M_\odot$ evolve until advanced phases of the core oxygen burning or the beginning of the

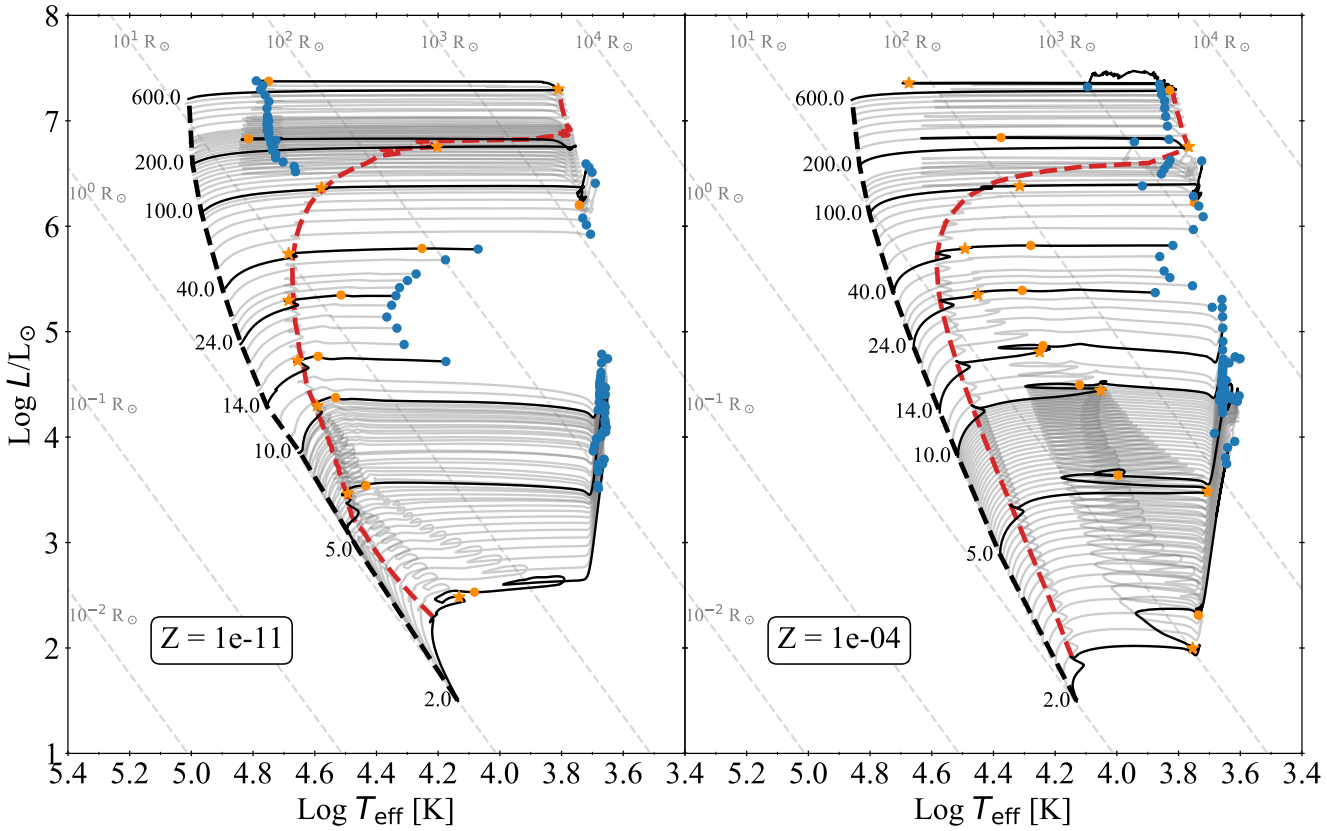

Figure 1. Hertzsprung–Russell (HR) diagram of Pop. III (left) and Pop. II (right) tracks. The black thick lines show the evolution of selected tracks with $M_{\rm ZAMS}$= 2, 5, 10, 14, 24, 40, 100, 200, and 600 M$_\odot$. All the other tracks are shown with solid grey lines. The dashed black line indicates the ZAMS. The red dashed line indicates the end of the MS. The orange stars (circles) mark the beginning (end) of core He burning. The blue circles indicate the final position of the star in the diagram before the supernova. Diagonal grey dashed lines correspond to constant stellar radii in R$_\odot$.

pair-instability regime. The Pop. III set of tracks extends the collection of PARSEC tracks, already used in SEVN (Iorio et al. 2023), and will soon be made available online[2].

We also computed new tracks of pure-He stars to extend the database to lower metallicities. We use tracks of pure-He stars to model naked-He stars formed via stripping during mass transfer at low metallicity (Kruckow et al. 2018; Spera et al. 2019; Mapelli et al. 2020; Iorio et al. 2023; Agrawal et al. 2023). The metallicity adopted is $Z = 10^{-6}$, and the masses range from $M_{\rm ZAMS,He} = 0.36$ to 350 M$_\odot$. This metallicity is similar to the metal content we find in He cores of Pop. III stars after the MS phase. For instance, depending on the initial mass, the carbon mass fraction in the He cores goes from 7×10^{-7} to 2.6×10^{-6} for 2 M$_\odot$ and 600 M$_\odot$, respectively. Therefore, we do not expect to have completely metal-free pure-He stars.

All the new tracks are computed with the same physical set-up as described in Costa et al. (2021, 2022) for stellar winds, nuclear reaction network, opacities, and equation of state. In Pop. III tracks, stellar winds are naturally quenched due to the lack of metals (particularly iron) which we accounted for (see Chen et al. 2015). Concerning the stellar convection, we adopt the Schwarzschild criterion (Schwarzschild 1958) for defining the unstable region and the mixing-length theory (Böhm-Vitense 1958) with a solar-calibrated value for the parameter $\alpha_{\rm MLT} = 1.74$ (Bressan et al. 2012). Above the convective core, we adopt a penetrative overshooting with a characteristic parameter of $\lambda_{\rm ov} = 0.5$ in units of pressure scale height, computed with the ballistic approach (Bressan et al. 1981). In this framework, $\lambda_{\rm ov}$ is the mean free path of the unstable element across the border of the convective region, and its value corresponds to about $f_{\rm ov} = 0.025$ in the exponential decay overshooting formalism (in the diffusive scheme, Herwig et al. 1997). We also included undershooting at the bottom of the convective envelope, with a characteristic distance of $\Lambda_{\rm env} = 0.7$ in pressure scale heights. The undershooting could play a role in the ending fate of massive stars, triggering dredge-up episodes which may stabilize the star against pair instability (Costa et al. 2021; Volpato et al. 2023). In the interpolation methods used in SEVN (described in detail in Iorio et al. 2023), we cut the evolution just before the early-AGB or the ignition of core C burning.

Figure 1 shows the two sets of tracks used in this work, Pop. III and II stars, in the Hertzsprung–Russell (HR) diagram. Pop. III stars begin their life as metal-free objects and, in the ZAMS, are more compact and hotter than their Pop. II counterparts.

Both Pop. III and Pop. II stars evolve towards the red part of the diagram during the MS. Figure 1 also shows a clear trend of the star

[2] http://stev.oapd.inaf.it/PARSEC

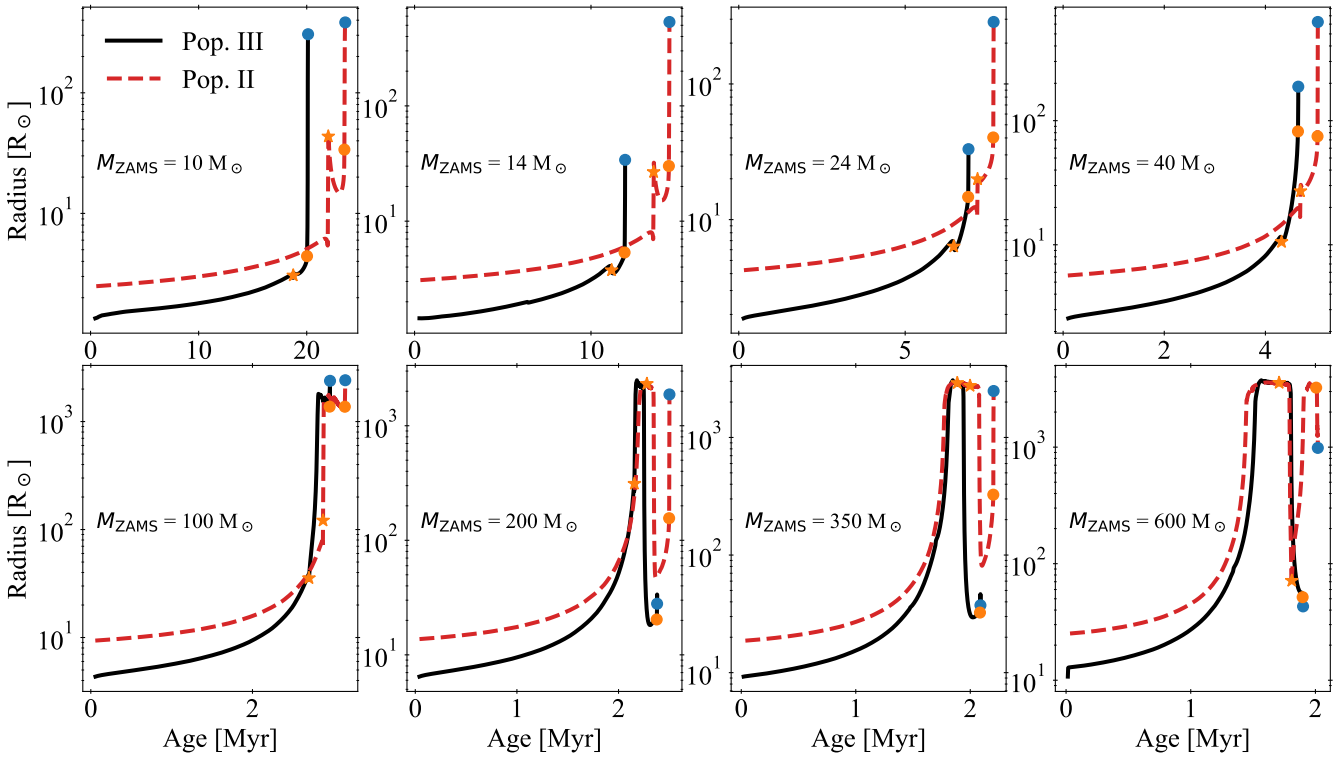

Figure 2. Radius versus age of some selected massive stars ($M_{ZAMS} \geq 10$ M$_\odot$). The solid black (dashed red) lines indicate Pop. III (Pop. II) stars. The orange stars (circles) mark the beginning (end) of core He burning. The blue circles indicate the final radius of the star before the supernova.

position at the end of the MS as a function of the initial stellar mass. Pop. III stars with an $M_{ZAMS} \leq 200$ M$_\odot$ end the MS as blue super-giant (BSG) stars, while, stars with $M_{ZAMS} > 200$ M$_\odot$ complete the MS as yellow super-giant (YSG) or red super-giant (RSG) stars. This trend is similar in Pop. II stars, but with a lower transition mass (about 150 M$_\odot$). Such a trend for Pop. III stars has also been found by other authors (e.g., Tanikawa et al. 2021b), but for higher initial masses ($M_{ZAMS} > 600$ M$_\odot$). Stars that become RSG during the MS develop large convective envelopes, differently from stars that remain BSG, which have mostly radiative envelopes. The transition mass that separates the two evolutionary pathways depends on the convection treatment adopted. This peculiar evolution of the most massive Pop. III and Pop. II stars can dramatically affect the evolution of a binary system since they become giant stars with very large radii during the MS, in which there is still no well-defined transition between the core and the envelope. Therefore, binary interactions in such cases may lead to early mergers.

The post-MS evolution of Pop. III stars shows several features in the HR diagram, which depend on M_{ZAMS}. Due to the high central temperatures during the MS, all the tracks ignite helium as BSG stars shortly after the end of the MS. Stars with a mass $M_{ZAMS} \leq 40$ M$_\odot$ end the CHeB phase in the blue side of the HR diagram. After the CHeB phase, stars with an initial mass between $2 \leq M_{ZAMS}/\mathrm{M}_\odot \leq 10$ evolve to the AGB. Stars above 10 M$_\odot$ evolve through all the advanced phases up to the oxygen burning, but they die with different final configurations. Stars in the mass range $10 < M_{ZAMS}/\mathrm{M}_\odot < 14$ move to the red part of the HR diagram and explode as RSG. Stars in the mass range $14 \leq M_{ZAMS}/\mathrm{M}_\odot \leq 40$ die as BSG. Similar behaviour in this mass range has been found by other authors (e.g. Marigo et al. 2001; Tanikawa et al. 2021b). Stars in the mass range $40 < M_{ZAMS}/\mathrm{M}_\odot \leq 100$ deplete helium in the red part of the diagram and finish their evolution as RSGs. Finally, stars with $M_{ZAMS} > 100$ M$_\odot$ ignite helium as RSGs, become BSGs during the CHeB, and remain BSGs until their final fate.

Concerning Pop. II stars, intermediate-mass stars ($2 \leq M_{ZAMS}/\mathrm{M}_\odot < 10$) do a blue loop during the CHeB, and then, after helium depletion, move to the AGB phase. Stars in the mass range $10 < M_{ZAMS}/\mathrm{M}_\odot \leq 100$ burn helium as BSGs before moving to the red part of the diagram. While stars with an initial mass $M_{ZAMS} \geq 100$ M$_\odot$ ignite helium as RSGs, burn it as BSGs (blue loop again), and later move back to the red. All massive stars ($M_{ZAMS} \geq 10$ M$_\odot$) burn all the elements up to oxygen and finally explode as RSGs.

Figure 2 shows the comparison between the radius evolution of Pop. III and Pop. II stars. Pop. III stars with $M_{ZAMS} \leq 100$ M$_\odot$ evolve and reach the RSG stage before Pop. II stars. Pop. III and Pop. II stars with a mass of ≥ 200 M$_\odot$ become RSGs with comparable timescales. Figure 2 shows that Pop. III stars with mass $M_{ZAMS} > 100$ M$_\odot$ reach the pre-supernova stage as compact BSGs stars, whereas Pop. II stars explode as very large RSG stars. Pop. III stars evolve to the final pre-supernova stage faster than Pop. II stars.

2.3 Binary initial conditions

In this Section, we describe the initial conditions used in this work for computing binary-population catalogues.

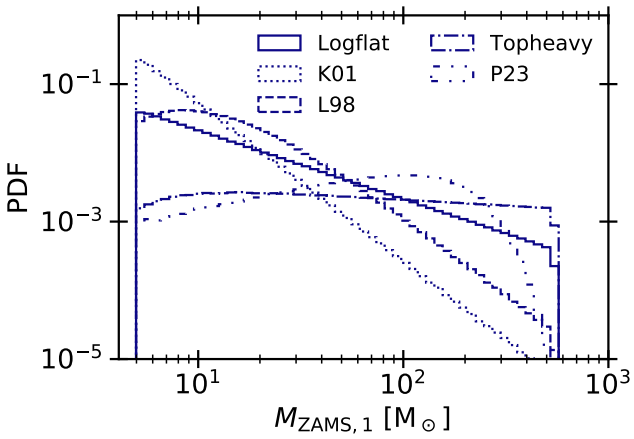

Figure 3. Initial mass distribution of the primary star ($M_{\rm ZAMS,1}$) in our models, as described in Section 2.3.1 and Table 1.

2.3.1 *Initial mass function (IMF)*

There is still no consensus about the initial mass function (IMF) of Pop. III stars, although several papers suggest that it should be rather top-heavy with respect to that of local stars (e.g., Chiosi et al. 1998; Abel et al. 2002; Bromm & Larson 2004; Yoshida et al. 2006; Bromm 2013; Glover 2013; Goswami et al. 2022). The transition between a top-heavy and a bottom-heavy mass function likely happened in the metallicity range of Pop. II stars (Chon et al. 2021; Sharda & Krumholz 2022). Here, given the uncertainties, we consider the same set of possible IMFs for both Pop. III and Pop. II stars, as follows.

- A *flat-in-log* distribution (Stacy & Bromm 2013; Susa et al. 2014; Hirano et al. 2014, 2015; Wollenberg et al. 2020; Chon et al. 2021; Tanikawa et al. 2021b; Jaura et al. 2022; Prole et al. 2022):

$$\xi(M_{\rm ZAMS}) \propto M_{\rm ZAMS}^{-1}. \tag{3}$$

This IMF will be our fiducial model for Pop. III stars.

- A Kroupa (2001) IMF (hereafter, K01):

$$\xi(M_{\rm ZAMS}) \propto M_{\rm ZAMS}^{-2.3}. \tag{4}$$

This mass function is often adopted for stars in the low-redshift Universe and will be our fiducial model for Pop. II stars. With respect to the original K01, which has a flatter slope for $M_{\rm ZAMS} < 0.5$ M$_\odot$, here we assume a single slope because we do not generate ZAMS masses < 5 M$_\odot$ from this distribution.

- A Larson (1998) distribution (hereafter, L98):

$$\xi(M_{\rm ZAMS}) \propto M_{\rm ZAMS}^{-2.35}\, e^{-M_{\rm cut1}/M_{\rm ZAMS}}, \tag{5}$$

where $M_{\rm cut1} = 20$ M$_\odot$ (Valiante et al. 2016).

- A *top-heavy* distribution (Stacy & Bromm 2013; Jaacks et al. 2019; Liu & Bromm 2020a):

$$\xi(M_{\rm ZAMS}) \propto M_{\rm ZAMS}^{-0.17}\, e^{-M_{\rm cut2}^2/M_{\rm ZAMS}^2}, \tag{6}$$

where $M_{\rm cut2} = 20$ M$_\odot$.

- The distribution derived by Park et al. (2023, hereafter, P23), based on hydro-dynamical simulations of Pop. III star formation, including radiative feedback from proto-stars and a diffuse weak X-ray background (see also Park et al. 2021a,b):

$$\xi(M_{\rm ZAMS}) \propto M_{\rm ZAMS}^{0.62} e^{-M_{\rm ZAMS}^2/M_{\rm cut3}^2}, \tag{7}$$

where $M_{\rm cut3} = 188$ M$_\odot$.

The IMF distributions adopted in this work are shown in Fig. 3.

2.3.2 *Mass ratio and secondary mass*

We draw the ZAMS mass of the secondary star ($M_{\rm ZAMS,\,2}$) according to three different distributions.

- We use the distribution of the mass ratio ($q = M_{\rm ZAMS,2}/M_{\rm ZAMS,1}$) from Sana et al. (2012, hereafter S12):

$$\xi(q) \propto q^{-0.1} \text{ with } q \in [0.1, 1] \text{ and } M_{\rm ZAMS,2} \geq 2.2\ {\rm M}_\odot. \tag{8}$$

This distribution is a fit to the mass ratio of O- and B-type binary stars in the local Universe (Sana et al. 2012).

- In the *sorted* distribution, we draw the ZAMS mass of the entire star population from the same IMF, and then we randomly pair two stars from this distribution, imposing that $M_{\rm ZAMS,2} \leq M_{\rm ZAMS,1}$. In this model, the minimum mass of the secondary is equal to that of the primary (5 M$_\odot$) by construction.

- The mass ratio distribution by Stacy & Bromm (2013, hereafter SB13):

$$\xi(q) \propto q^{-0.55} \text{ with } q \in [0.1, 1] \text{ and } M_{\rm ZAMS,2} \geq 2.2\ {\rm M}_\odot. \tag{9}$$

This distribution was obtained from a fit to Pop. III stars formed in cosmological simulations (SB13).

The final mass ratio distribution also depends on the mass distribution of the primary star, as shown in Fig. 4.

2.3.3 *Orbital period*

We consider two different distributions for the initial orbital period (P), as shown in the left-hand panel of Fig. 5:

- The distribution derived by S12 for O- and B- stars in the local Universe:

$$\xi(\Pi) \propto \Pi^{-0.55} \quad \text{with} \quad \Pi = \log(P/{\rm day}) \in [0.15, 5.5]. \tag{10}$$

- The period distribution found by SB13:

$$\xi(\Pi) \propto \exp\left[-(\Pi-\mu)^2/(2\,\sigma^2)\right]. \tag{11}$$

This is a Gaussian distribution with $\mu = 5.5$, and $\sigma = 0.85$, favouring long periods with respect to the S12 distribution. While this distribution is likely affected by numerical resolution, which reduces the number of systems with short orbital periods, we decide to consider it as a robust upper limit to the orbital period of Pop. III and II binary stars (see also Sugimura et al. 2020; Park et al. 2021b, 2023).

2.3.4 *Eccentricity*

We compare two distributions for the orbital eccentricity, as shown in the right-hand panel of Fig. 5:

- the distribution obtained by S12 and based on a sample of O- and B-type stars in the local Universe:

$$\xi(e) \propto e^{-0.42} \quad \text{with } e \in [0, 1). \tag{12}$$

- The thermal distribution, adopted for Pop. III binaries by, e.g., Kinugawa et al. (2014); Hartwig et al. (2016); Tanikawa et al. (2021b):

$$\xi(e) = 2\,e \quad \text{with } e \in [0, 1). \tag{13}$$

This eccentricity distribution favours highly eccentric systems, at variance with Eq. 12. Recent hydro-dynamical simulations (Park et al. 2021b, 2023) suggest that Pop. III binary stars form preferentially with high orbital eccentricity, favouring the distribution in Eq. 13 with respect to Eq. 12.

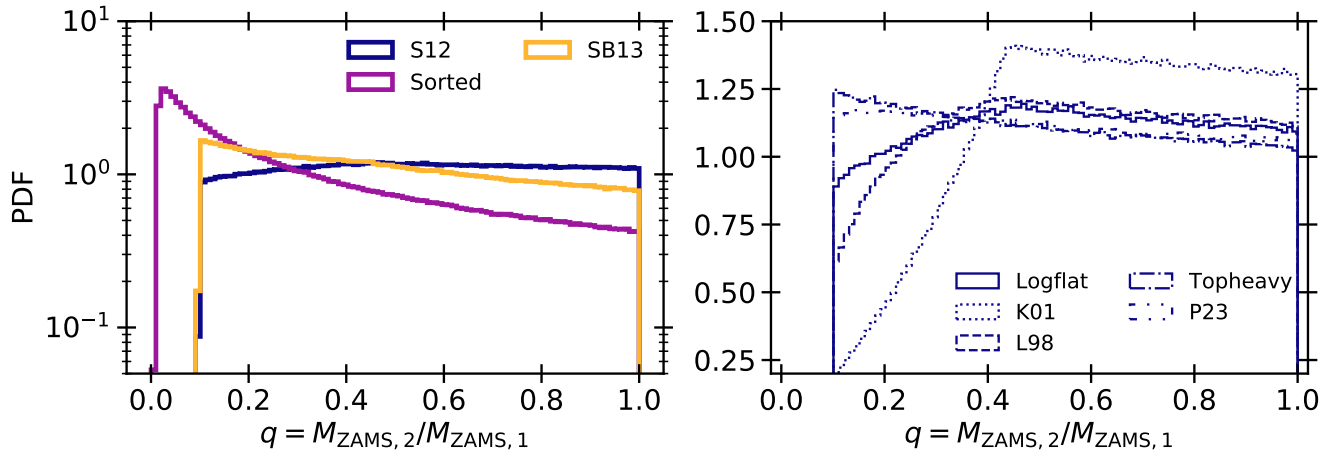

Figure 4. The left-hand panel shows our three initial mass-ratio ($q = M_{\rm ZAMS,2}/M_{\rm ZAMS,1}$) distributions (S12, Sorted, and SB13), calculated assuming a flat-in-log IMF for the primary mass. The right-hand panel shows the behaviour of the S12 mass-ratio distribution depending on the primary mass function (flat-in-log, K01, L98, top-heavy, and P23). The line style is the same as Fig. 3. See Table 1 for more details.

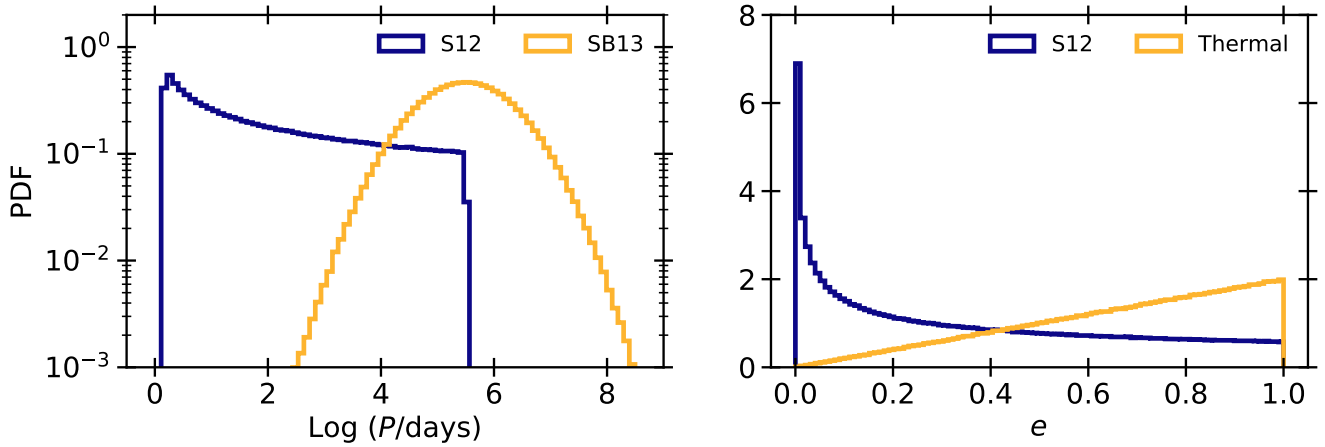

Figure 5. The left-hand and right-hand panels show the orbital period P and eccentricity e distributions adopted in our initial conditions (Table 1).

2.3.5 Input catalogues

We build 13 different input catalogues by varying the aforementioned distributions of the IMF, q, P, and e. For each of these catalogues, we consider the two metallicities for Pop. III and Pop. II, i.e. $Z = 10^{-11}$ and 10^{-4}, respectively.

We set the total number of generated binaries to obtain 10^7 binaries in the high-mass regime ($M_{\rm ZAMS,2} \geq 10$ M$_\odot$, and $M_{\rm ZAMS,1} \geq 10$ M$_\odot$ by construction). For the models that draw the primary mass from K01 and L98 (Section 2.3.1), we limit the total number of generated binaries to 2×10^7 (consisting of 10^7 binaries in the high- and low-mass range, respectively). As a consequence, the low-mass regime ($M_{\rm ZAMS,2} \leq 10$ M$_\odot$) is under-sampled by a factor of $\approx 4-5$ for K01 and $\lessapprox 1.2$ for L98. We take into account the incomplete sampling of the initial conditions by performing an a posteriori over-sampling of the simulated binaries with $M_{\rm ZAMS,2} \leq 10$ M$_\odot$. This ensures a good sampling of the high-mass regime and reduces stochastic fluctuations (e.g., Iorio et al. 2023).

Table 1 lists the properties of our input catalogues. We label our input catalogues by taking the IMF name and adding a number that indicates the distribution of mass ratios, periods, and eccentricities. Therefore, the LOG, KRO, LAR, TOP, and PAR catalogues adopt the flat-in-log, K01, L98, top-heavy, and P23 IMF, respectively.

In all our models but LOG3 (Table 1), we randomly sample the ZAMS mass of the primary star $M_{\rm ZAMS,1}$ (i.e., the ZAMS mass of the most massive member) of the binary system in the range [5, 550] M$_\odot$, according to one of the five aforementioned distributions. We then randomly sample the ZAMS mass of the secondary star ($M_{\rm ZAMS,2}$) based on the mass ratio distributions described in Section 2.3.2. We assume that the secondary mass can be as low as 2.2 M$_\odot$.

In model LOG3, we instead randomly sample the entire IMF in the range $M_{\rm ZAMS} \in$ [5, 550] M$_\odot$, according to the LOG distribution. We then randomly pair the generated stellar masses. The primary (secondary) star is thus the component with the higher (lower) initial mass (see model sorted in Section 2.3.2). Hereafter, we assume the models LOG1 and KRO1 as our fiducial case for Pop. III and Pop. II stars, respectively.

Table 1. Initial conditions.

Model	$M_{\rm ZAMS,1}$	$M_{\rm ZAMS}$	Mass ratio q	Period P	Eccentricity e	N [$\times 10^7$]	Total mass [$\times 10^9$ M$_\odot$]
LOG1	Flat in log	–	S12	S12	S12	1.45	2.59
LOG2	Flat in log	–	S12	SB13	Thermal	1.45	2.58
LOG3	–	Flat in log	Sorted	S12	S12	1.38	3.19
LOG4	Flat in log	–	SB13	S12	Thermal	1.53	2.60
LOG5	Flat in log	–	SB13	SB13	Thermal	1.53	2.60
KRO1	K01	–	S12	S12	S12	5.23 (2.00†)	1.35 (0.89†)
KRO5	K01	–	SB13	SB13	Thermal	6.11 (2.00†)	1.52 (0.93†)
LAR1	L98	–	S12	S12	S12	2.00	1.20
LAR5	L98	–	SB13	SB13	Thermal	2.27 (2.00†)	1.30 (1.24†)
TOP1	Top heavy	–	S12	S12	S12	1.05	4.16
TOP5	Top heavy	–	SB13	SB13	Thermal	1.07	4.03
PAR1	P23	–	S12	S12	S12	1.05	2.35
PAR5	P23	–	SB13	SB13	Thermal	1.06	2.28

Column 1 reports the model name. Columns 2 describes how we generate the ZAMS mass of the primary star (i.e., the most massive of the two members of the binary system). Column 3 describes how we generate the ZAMS mass of the overall stellar population (without differentiating between primary and secondary stars). We follow this procedure only for model LOG3 (see the text for details). Columns 3, 4, and 5 specify the distributions we used to generate the mass ratios, the orbital periods and the orbital eccentricity. See Section 2.3 for a detailed description of such distributions. The last two columns report the total number and the total mass of the of simulated binaries, respectively. †The ICs for such models are under-sampled, the actual number of simulated systems and their total mass is reported in parentheses. See main text for additional details.

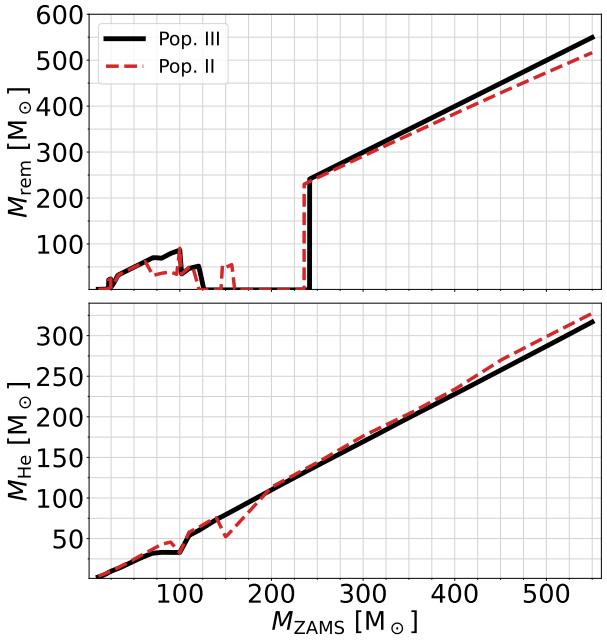

Figure 6. The upper and lower panel show the mass of the compact remnant, and the mass of the He core at the onset of core collapse as a function of the initial mass, $M_{\rm ZAMS}$. Black solid and red dashed lines refer to Pop. III and Pop. II stars, respectively.

3 RESULTS

3.1 Black holes from single star evolution

Figure 6 shows the mass of the compact remnant ($M_{\rm rem}$) as a function of the ZAMS mass ($M_{\rm ZAMS}$) for Pop. II and Pop. III stars evolved via single stellar evolution. Pop. II and III stars evolving via single star evolution produce similar He core masses and, thus, similar compact remnant masses. The only differences are (i) in the range between pulsational pair instability and pair instability ($M_{\rm ZAMS} \in$ [60, 170] M$_\odot$), where envelope overshooting can cause dredge-up episodes, and (ii) at extremely high BH masses ($M_{\rm rem} > 400$ M$_\odot$), where Pop. II stars suffer from slightly higher mass loss rates.

In the region between pulsational pair instability and pair instability ($M_{\rm ZAMS} \in$ [60, 170] M$_\odot$), the He-core mass does not grow monotonically, especially in the case of Pop. II stars. The core decrease in some mass ranges is caused by dredge-up episodes triggered by envelope undershooting (Costa et al. 2021). Different choices for the convection parameters, such as the core overshooting ($\lambda_{\rm ov} = 0.5$ in our models), can change the behaviour and the occurrence of dredge-up episodes. For instance, Pop. II stars (Z = 0.0001) with $\lambda_{\rm ov} = 0.4$ show a monotonic trend of the He core mass (see discussion in Iorio et al. 2023). In the models presented in this work, for ZAMS mass $M_{\rm ZAMS} \in [145 - 160]$ M$_\odot$ we expect an "island" of massive BH formation for Pop. II stars inside a region of pair instability. This happens because a dredge-up episode reduces the mass of the He and CO core below the threshold for pair instability in this range for Pop. II stars, but not for Pop. III stars.

The maximum mass of a Pop. III BH below the pair-instability mass gap is 86 M$_\odot$ for the adopted pair-instability model. Similarly, the maximum mass of a Pop. II BH below the mass gap is 91 M$_\odot$. In both cases, this mass is reached for a ZAMS mass $\approx 100 - 105$ M$_\odot$. Below the mass gap, our models predict several sharp features in the BH mass spectrum because of dredge-up episodes that affect the He core mass in this range. The mass spectrum in this region is maximally sensitive to several details of the input physics that are highly uncertain (e.g., core overshooting, nuclear reaction rates), as already discussed in previous papers (e.g., Leung et al. 2019; Farmer et al. 2019, 2020; Mapelli et al. 2020; Costa et al. 2021; Woosley & Heger 2021; Vink et al. 2021).

In our models, the upper edge of the mass gap is at $M_{\rm ZAMS} \approx 242$ M$_\odot$ and ≈ 236 M$_\odot$ for Pop. III and II stars, respectively. Above the

mass gap, both Pop. III and II stars produce intermediate-mass BHs from direct collapse. The mass of a BH born from a Pop. III star in this regime is very similar to that of a BH formed by a Pop. II star with the same ZAMS mass, because stellar winds are already extremely quenched at $Z = 10^{-4}$.

The maximum BH mass in our models is $M_{\rm rem} \approx 545$ M$_\odot$ (≈ 510 M$_\odot$) for Pop. III (Pop. II) stars, corresponding to a ZAMS mass $M_{\rm ZAMS} = 550$ M$_\odot$. We obtain these masses with the optimistic assumption that the residual H-rich envelope of the progenitor star collapses to a BH entirely when the star collapses. A fraction of the H-rich envelope mass might be lost even in the case of a failed explosion, because of shocks induced by the emission of neutrinos (e.g., Fernández et al. 2018; Renzo et al. 2020b).

3.2 Binary evolution

Figures 7 and 8 show the secondary BH mass (i.e. the mass of the least massive BH) versus the primary BH mass (i.e. the mass of the most massive BH) for all our simulated BBH mergers. The masses of BBHs born from Pop. III stars are qualitatively similar to those of BBHs born from Pop. II stars, for all the considered models.

Mergers with at least one component above the pair-instability mass gap are not common, and mergers inside the gap are even rarer. In our binary simulations, it is even difficult to identify sharp edges for the pair instability mass gap, because of dredge-up episodes and mass transfer (Figure 9). Assuming that the pair-instability mass gap spans from 85 to 230 M$_\odot$, we find that BBH mergers with primary BH masses above the gap are up to 3.3% (LOG3) and up to 0.09% (TOP5) for Pop. III and Pop. II stars, respectively. With the same definition, mergers with primary BH mass inside the gap are up to 1.9% (LOG3) and up to 2.4% (TOP5) for Pop. III and Pop. II stars, respectively. In general, Pop. II stars seem to produce more BBH mergers with primary BH mass above the gap with respect to Pop. III stars, with the exception of model LOG3 (Fig. 9). Furthermore, no secondary BHs in our BBH mergers have mass inside or above the gap.

The most common primary BH masses are around 30–40 M$_\odot$ (Fig. 9). There is a dearth of low-mass primary BHs ($8-10$ M$_\odot$) with respect to LVK mergers (Abbott et al. 2019, 2021c, 2023) in all of our runs, even KRO1. This is a consequence of the negligible mass loss rate and relatively compact stellar radii at such low metallicity.

Our models show a preference for equal mass systems but also a non-negligible contribution from unequal mass mergers (Figs. 7 and 8). The secondary BH mass is always $M_{\rm s} \leq 45$ M$_\odot$ for both Pop. II and III stars. Figure 10 highlights some differences between Pop. II and III BBHs. For example, the most common secondary BH mass for Pop. III stars is ~ 20 M$_\odot$, while for Pop. II stars it is either $\sim 8-10$ M$_\odot$ (KRO1, LAR1), or $\sim 35-38$ M$_\odot$ (LOG2, LOG5, TOP5), depending on the model.

We find another interesting difference between Pop. III and II BBHs if we look at the mass ratio (Fig. 11). In the case of Pop. II stars, equal-mass BBHs are the most common systems regardless of the model, even if models LOG5, KRO5, LAR5, TOP5 and PAR5 show a mild secondary peak for $q \sim 0.4-0.5$. In contrast, for Pop. III stars, the most common BBH mass ratio is $\sim 0.8-0.9$ for the models LOG1, LOG3, LOG4, KRO1, LAR1, TOP1 and PAR1, i.e. for all the models adopting the S12 initial period distribution. This is a consequence of the dominant evolutionary channels in such models (see Section 4.1).

Finally, the distribution of delay times $t_{\rm del}$ (i.e., the time elapsed between the formation of the binary system and the BBH merger) shows another difference between Pop. III and II BBHs (Fig. 12).

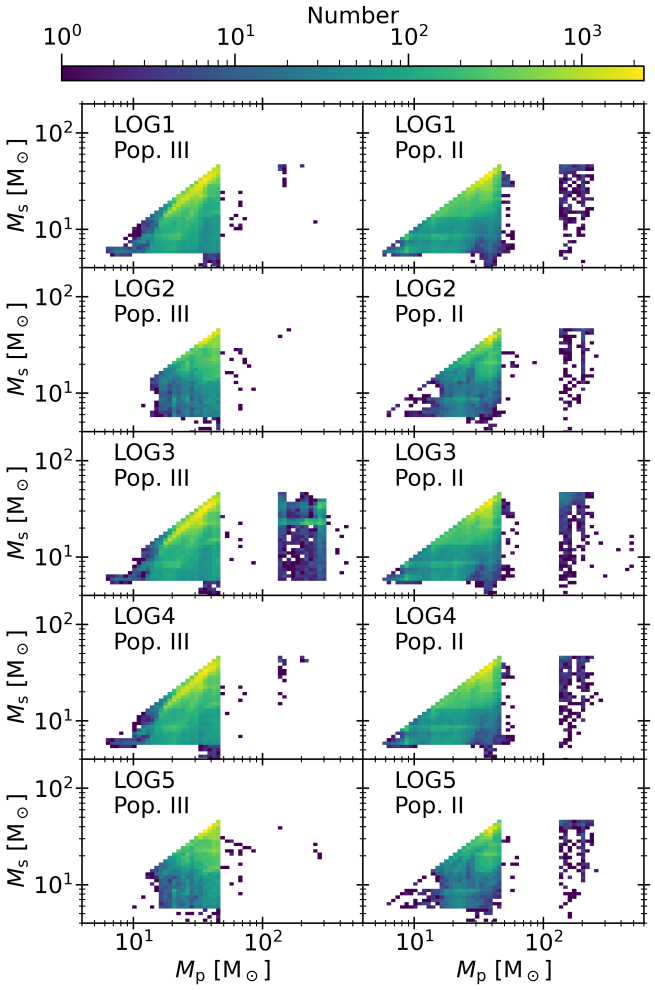

Figure 7. Distribution of secondary ($M_{\rm s}$) versus primary ($M_{\rm p}$) mass of all BBH mergers in our simulations LOG1–5. Left (Right): Pop. III (II) stars. The colour bar indicates the number of BBHs in each cell.

All Pop. III models seem to match the trend $t_{\rm del} \propto t^{-1}$ between 3 and 10^4 Myr. In contrast, some of the Pop. II models (LOG2, LOG5, KRO5, LAR5, TOP5 and PAR5) show an excess of short delay times ($3-10$ Myr). The models showing this excess share the SB13 orbital period distribution. This feature is another signature of the formation channel, as we discuss in Section 4.1.

4 DISCUSSION

4.1 Formation channels of BBH mergers

The features of BBH mergers we described in the previous section (Section 3.2) can be interpreted by looking at the formation channels of our BBHs. Figure 13 summarizes the main formation channels of BBH mergers from Pop. III and Pop. II stars. Tables 2 and 3 report the percentages in detail.

We distinguish five main channels, following the definition by Iorio et al. (2023). BBH mergers that go through Channel 0 do not undergo any mass transfer episodes during the evolution of their progenitors. Systems belonging to this channel are always very rare ($\ll 1\%$). Since this channel is so uncommon, we do not show it in Figure 13 and in the following Figures.

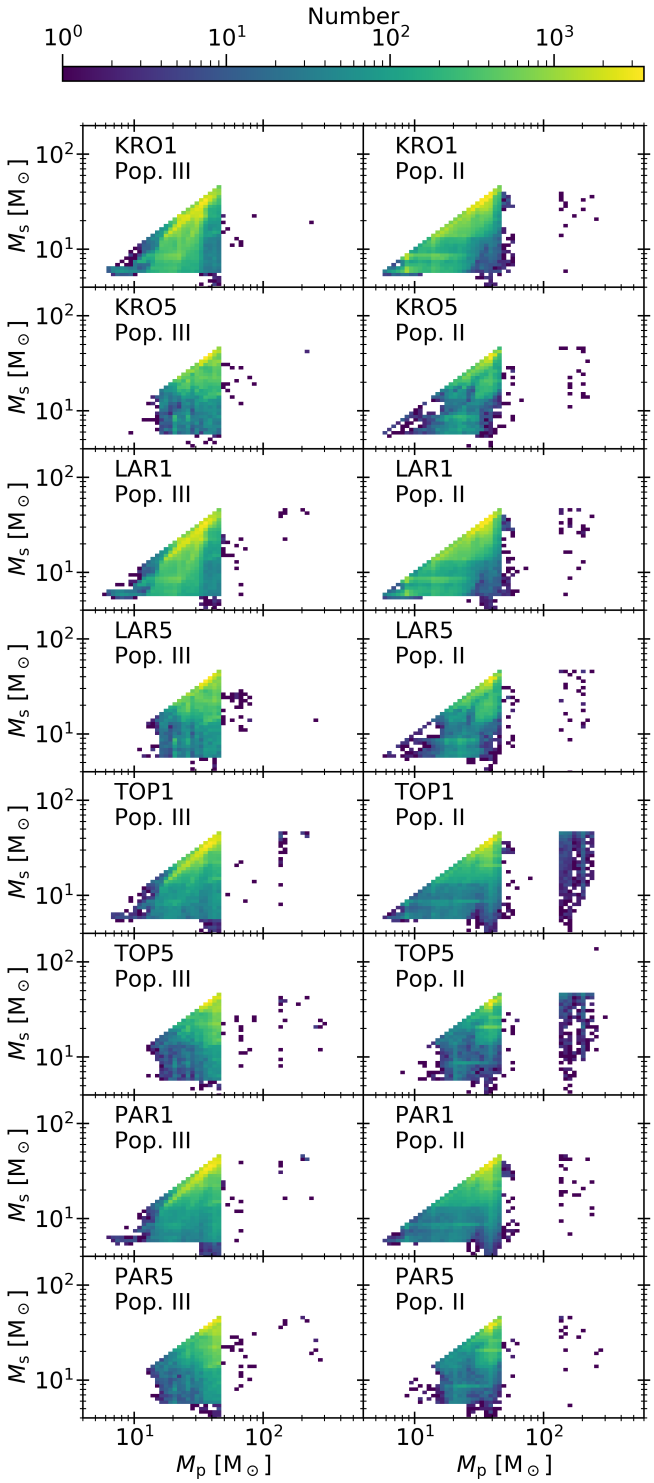

Figure 8. Same as Fig. 7 but for models KRO1, KRO5, LAR1, LAR5, TOP1, TOP5, PAR1, and PAR5

.

Table 2. Percentage of BBH mergers from Pop. III stars.

Model	BBHm [%]	Ch. 0 [%]	Ch. I [%]	Ch. II [%]	Ch. III [%]	Ch. IV [%]
LOG1	11.25	0.1	3.65	74.81	7.62	13.71
LOG2	0.75	0.22	3.3	1.27	58.77	36.11
LOG3	9.33	0.09	3.35	70.41	17.31	8.76
LOG4	11.57	0.12	3.26	67.57	18.13	10.69
LOG5	0.68	0.23	3.3	1.52	64.6	30.07
KRO1	14.66	0.19	1.93	85.82	4.08	7.7
KRO5	0.85	0.34	2.04	2.18	65.11	29.35
LAR1	14.34	0.16	2.13	83.57	4.89	9.03
LAR5	0.91	0.38	2.26	1.98	64.97	29.74
TOP1	6.47	0.06	5.65	66.17	10.39	17.67
TOP5	0.36	0.19	4.47	1.26	64.81	29.14
PAR1	12.05	0.05	6.45	62.22	11.65	19.59
PAR5	1.11	0.13	4.28	1.07	64.93	29.53

Column 1: Model; column 2: percentage of BBH mergers with respect to all simulated BBHs; columns 3, 4, 5, 6, and 7: BBH mergers formed via channel 0, I, II, III, and IV, respectively.

Table 3. Percentage of BBH mergers from Pop. II stars.

Model	BBHm [%]	Ch. 0 [%]	Ch. I [%]	Ch. II [%]	Ch. III [%]	Ch. IV [%]
LOG1	13.53	0.02	5.94	70.48	7.59	15.44
LOG2	0.97	0.12	1.3	1.44	48.11	45.88
LOG3	10.88	0.03	5.98	70.55	12.34	10.71
LOG4	14.46	0.02	4.03	67.06	13.37	14.79
LOG5	0.86	0.11	1.48	1.53	54.96	39.05
KRO1	16.23	0.03	6.16	79.64	2.85	10.01
KRO5	1.15	0.23	0.79	1.66	41.21	45.93
LAR1	16.15	0.04	5.28	78.93	3.37	11.35
LAR5	1.16	0.22	0.91	1.6	43.11	46.57
TOP1	8.52	0.02	7.42	59.61	14.73	17.99
TOP5	0.48	0.1	1.9	1.44	64.8	30.76
PAR1	15.13	0.01	8.53	58.46	12.52	20.32
PAR5	1.36	0.06	2.01	1.48	61.36	34.33

Column 1: Model; column2: percentage of BBH mergers with respect to all simulated BBHs; columns 3, 4, 5, 6, and 7: BBH mergers formed via channel 0, I, II, III, and IV, respectively.

Channel I is often referred to as the "traditional" formation channel of BBH mergers: the two progenitor stars undergo stable mass transfer before the formation of the first BH. Then, after the formation of the first BH, the system evolves through at least one common envelope.

In channel II, the system evolves only via stable mass transfer episodes. Finally, in both channel III and IV, the system undergoes at least one common envelope before the formation of the first BH. The only difference between channel III and IV is that in the former the companion star preserves a residual of the original H-rich envelope at the time of the formation of the first BH, while in the latter the companion has already been stripped of its envelope when the first BH forms.

The initial orbital period is the main driver of the relative differences among formation channels (Fig. 13). As we detail below, relatively short initial orbital periods (as in S12) favour channel II (i.e. stable mass transfer), while relatively long initial orbital periods (SB13) favour channels III and IV (i.e., formation channels with a common-envelope episode before the formation of the first BH). The main reason is that for short initial orbital periods the two progenitor

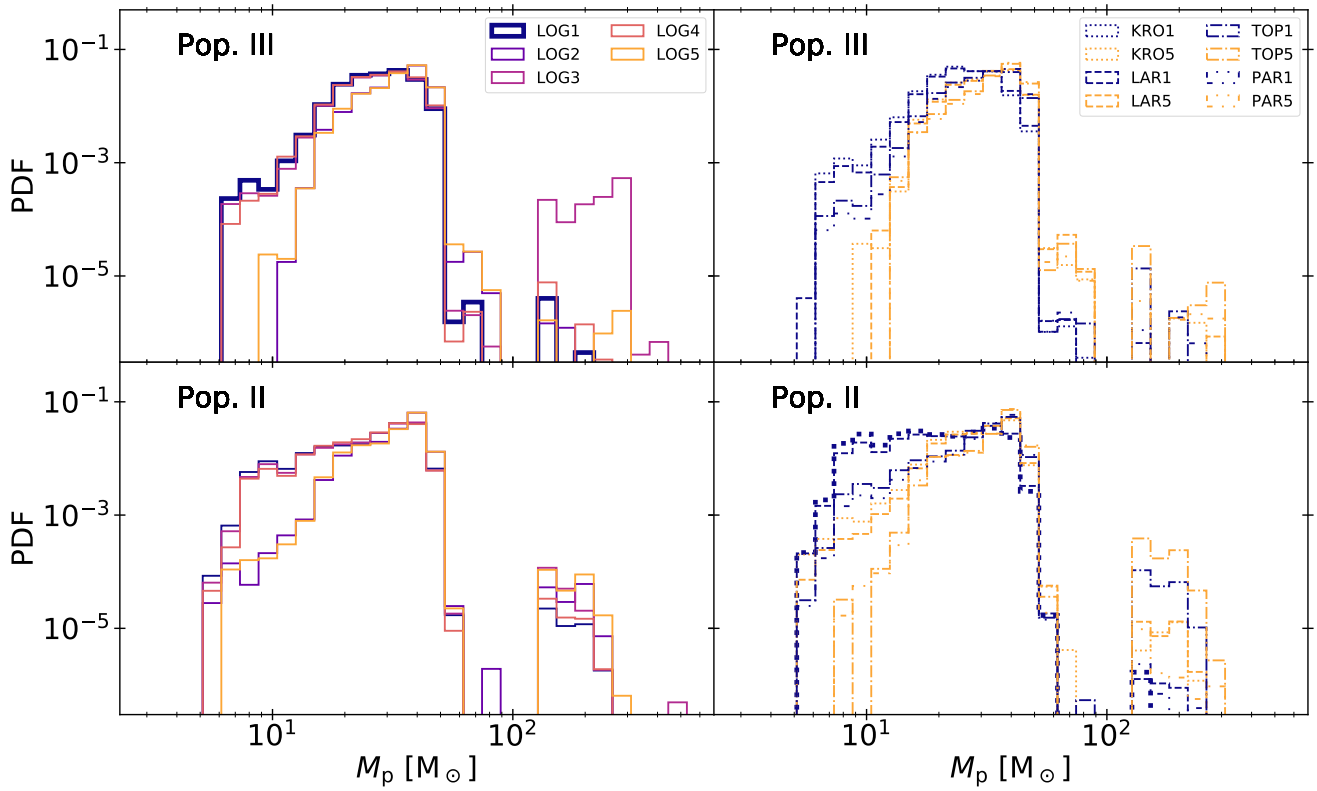

Figure 9. Distribution of the primary BH mass (i.e., the most massive BH in each binary system) in the simulated BBH mergers. Upper (lower) panel: Pop. III (Pop. II) stars. The left-hand panels show the models with the flat-in-log IMF, while the right-hand panels show all the other models. The fiducial models (i.e. LOG1 for Pop. III and KRO1 for Pop. II stars) are highlighted with a thicker line.

stars undergo the first stable mass transfer episode early in their life (during the MS or Hertzsprung-gap phase), while for large initial orbital periods the first interaction happens in a late evolutionary phase, when the primary star has developed a large radius and a well-defined core structure. This result holds for both Pop. III and Pop. II stars (Fig. 13).

Figures 14 and 15 show the behaviour of Pop. III BBHs and their progenitor stars in models LOG1 and LOG5, respectively. We show only models LOG1 and LOG5 for the sake of brevity: Models LOG3, LOG4, KRO1, LAR1, TOP1 and PAR1 behave in a similar way to LOG1 with respect to the formation channels (these are the models that adopt the initial S12 orbital period distribution), while models LOG2, KRO5, LAR5, TOP5, and PAR5 behave in a similar way to LOG5, which adopts the initial SB13 orbital period distribution.

Channel II (i.e. stable mass transfer) is the dominant channel for model LOG1 and for all the other models that adopt the initial S12 distribution of the orbital periods. Figure 14 shows that most channel II systems are associated with short initial semi-major axis $a = 10-10^3$ R$_\odot$. These short initial semi-major axes are heavily suppressed with the orbital period distribution by SB13 (Fig. 15).

Figure 14 also shows that channel II is associated with relatively low mass ratios in the ZAMS ($q_{\rm ZAMS} \sim 0.5-0.9$) and relatively low mass ratios between the two final BHs ($q_{\rm BH} = 0.75-0.9$) for Pop. III stars. Hence, the predominance of channel II in the models adopting the S12 orbital period distribution explains why these models have a preference for BBH mass ratios $q_{\rm BH} = 0.75-0.9$ in the case of Pop. III stars, as discussed in the previous Section (Fig. 11). In these systems, the mass difference between primary and secondary stars is sufficiently large that the system undergoes the first mass transfer while the secondary is still on the MS.

In contrast, channels III and IV are the dominant channels for all the models that adopt the SB13 orbital period distribution. As shown by, e.g., Fig. 15, the large initial semi-major axes of distribution SB13 suppress systems with initial orbital separation $a < 10^3$ R$_\odot$, hence suppressing channel II. Channel III and IV preferentially arise when $a \sim 10^3 - 10^5$ R$_\odot$. In this case, mass transfer takes place only when the radii of the two stars become very large, i.e. in the late evolutionary stages. Channel IV is the preferred channel of equal-mass stars, that evolve nearly at the same time and strip off each other's envelopes. It mainly leads to the formation of equal-mass BBHs, explaining the preference of these models for equal-mass mergers (Fig. 11). In contrast, channel III has a preference for markedly unequal-mass systems, explaining the population of BBHs with $q \leq 0.6$ in models LOG5, KRO5, LAR5, TOP5, and PAR5 (especially for Pop. II stars, Fig. 11).

Figure 16 compares the properties of BBH mergers from Pop. III and Pop. II stars in the case of model KRO1 (the fiducial model for Pop. II stars). Since channels I and III are less important than channels II and IV in this model, we show only the latter channels for simplicity. This Figure shows that Pop. III and Pop. II stars have a very similar behaviour in the case of channel IV. As for channel II, we see three main differences: Pop. II stars have a preference for i) higher ZAMS mass $M_{\rm ZAMS}(M_{\rm p})$, ii) larger mass ratios in the ZAMS $q_{\rm ZAMS}$, and iii) and larger BBH mass ratios $q_{\rm BH}$ with respect to Pop. III stars. The correlation between these three properties explains

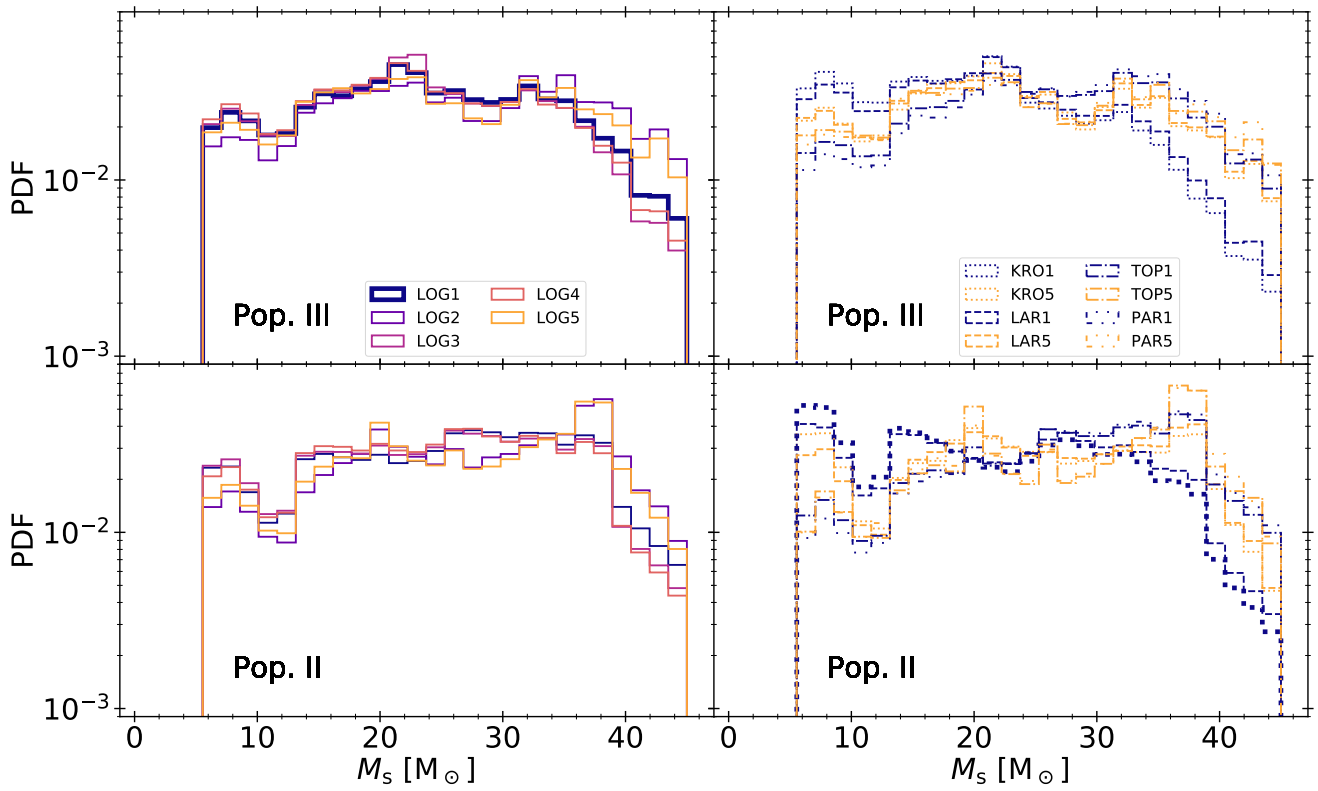

Figure 10. Same as Fig. 9, but for the secondary BH mass (i.e., the least massive BH of each binary system).

why Pop. II stars tend to produce equal-mass BBHs, while Pop. III stars produce BBHs with a mass ratio peaking at $q_{\rm BH} \approx 0.8$ (Fig. 11).

Figure 17 compares the delay time distribution of Pop. III and Pop. II binary systems if we consider models KRO1 (fiducial model for Pop. II), LOG1 (fiducial model for Pop. III), LOG5 and KRO5. Channel IV is skewed toward the shortest delay times, for both Pop. III and II binary stars, because it is associated with the most efficient orbital shrinking during common envelope. The shrinking is more efficient for Pop. II stars (especially in models LOG5 and KRO5), because they reach even larger radii in their late evolutionary stages (see Figures 1 and 2). This explains why the overall delay time distribution of Pop. II systems (Figure 12) has an excess at very low values ($t_{\rm del} \leq 10$ Myr) in models LOG2, LOG5, KRO5, LAR5, TOP5, and PAR5. In contrast, channel II is associated with long delay times, because stable mass transfer is not as efficient as common envelope in reducing the orbital separation.

Tables 2 and 3, and Figure 13 show that both Pop. III and Pop. II stars behave in a very different way from more metal rich binary systems. In fact, only $\lesssim 5.7\%$ ($\lesssim 7.5\%$) of all BBH mergers evolve via channel I in the case of Pop. III (II) binary stars. For comparison, Iorio et al. (2023) show that between 50 and 80% of all BBH mergers evolve via channel I at metallicity between $Z = 2\times10^{-3}$ and $Z = 10^{-2}$ (see Fig. 14 of Iorio et al. 2023 for $\alpha = 1$).

The abundance of channel II systems and the dearth of channel I systems for Pop. III and II binary stars with respect to metal-rich binary systems ($Z \in [2\times10^{-3} - 10^{-2}]$) are a consequence of the large BH masses at such low metallicity. In fact, both channel I and II systems go through a stable mass transfer before the formation of the first compact object, and then undergo a second mass transfer after the formation of the first compact object. The only difference between the two channels is that the mass transfer episode between the companion star and the first-born BH becomes unstable in channel I and remains stable in channel II. In SEVN (as in most binary population-synthesis codes) the stability of mass transfer is evaluated through a critical mass ratio $q_{\rm crit}$ between the donor and the accretor: the systems with mass ratio $q \geq q_{\rm crit}$ undergo a dynamically unstable mass transfer (i.e., a common-envelope episode), while mass transfer remains stable in the other cases (Hurley et al. 2002). Since most our Pop. II and III BHs in tight binary systems are relatively massive ($\gtrsim 20$ M$_\odot$, Fig. 6), we have that $q < q_{\rm crit}$ in most binary systems (where q is the mass ratio between the donor star and the first born BH), ensuring the stability of most mass-transfer episodes.

Furthermore, the abundance of channel II versus channel I systems depends on the assumed value of common-envelope efficiency $\alpha_{\rm CE}$. We have re-run the fiducial case LOG1 with $\alpha_{\rm CE} = 3$. We find that for Pop. III stars, the percentage of channel II systems decreases from 75% for $\alpha_{\rm CE} = 1$ down to 51% for $\alpha_{\rm CE} = 3$. This happens because, when $\alpha_{\rm CE}$ is large, the common envelope process is less efficient in shrinking the orbital separation. In contrast, the relative abundance between channel I and II systems is not significantly affected by our assumption that mass transfer is always stable for MS and Hertzsprung-gap donors. In fact, both channels I and II undergo a stable mass transfer when the primary star is still a MS or an Hertzsprung-gap star. Relaxing the aforementioned assumption has a more sizable impact on the evolution of channels III and IV systems, which evolve via common envelope before the formation of the first-born BH.

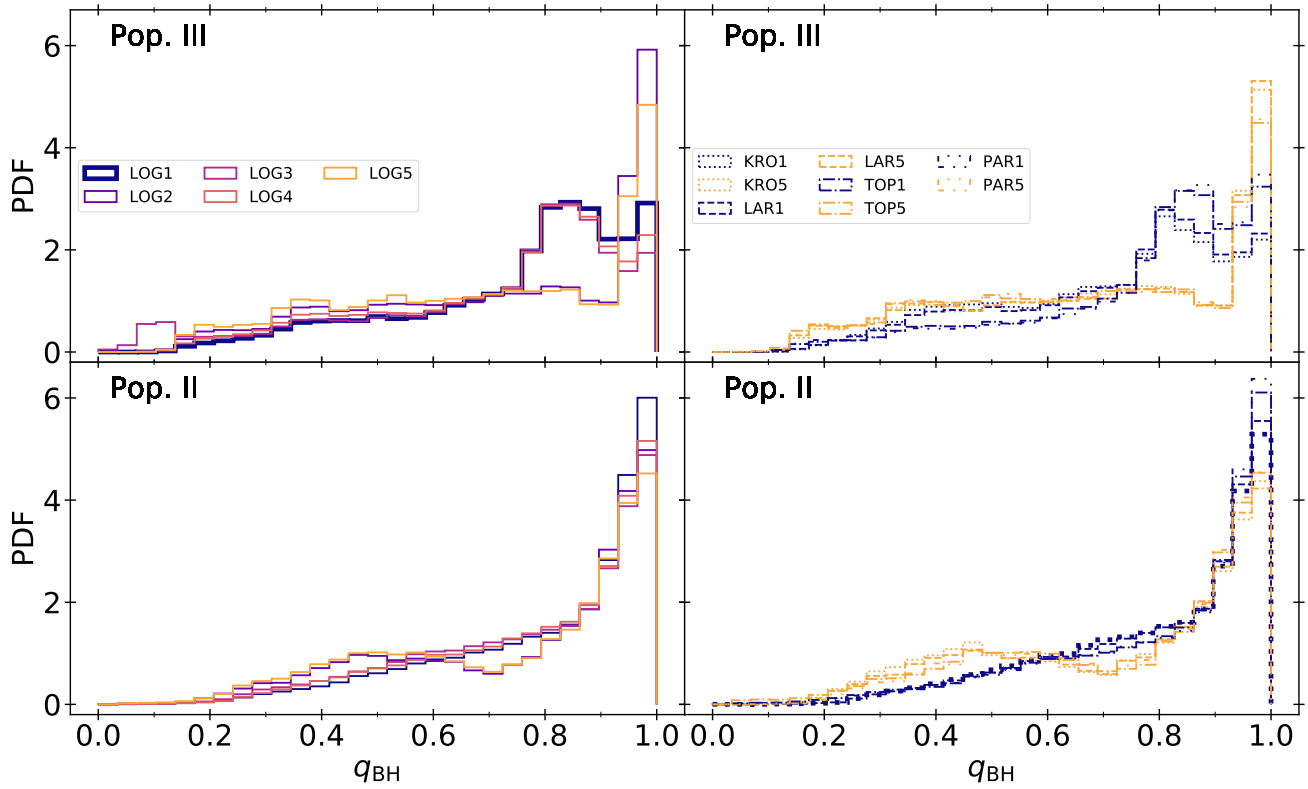

Figure 11. Same as Fig. 9, but for the mass ratio $q_{\rm BH} = M_{\rm s}/M_{\rm p}$ between the secondary and primary BH.

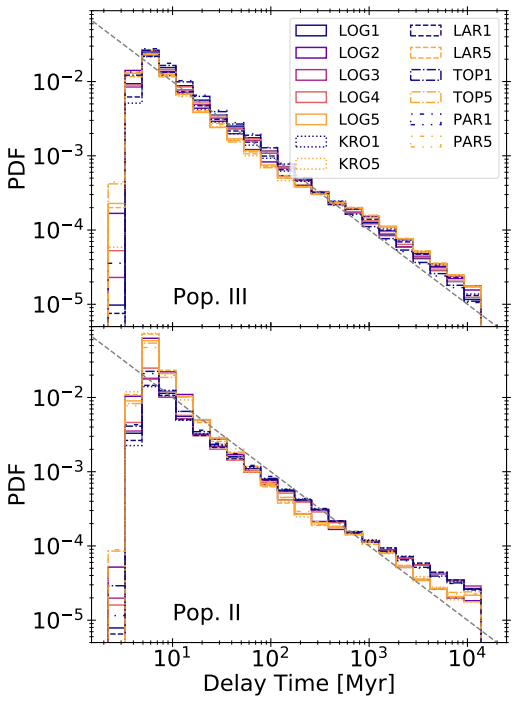

Figure 12. Distribution of delay times, i.e. the time elapsed from the formation of the binary star to the merger of the two BHs. The gray dashed line shows the $\propto t^{-1}$ predicted trend (e.g., Dominik et al. 2012).

4.2 BBH mergers with primary above the mass gap

Channel III is the key to interpret the abundance of BBHs with primary mass above the gap in model LOG3. These systems are associated with a population of binary stars with very low $q_{\rm ZAMS}$ (Figure 18), mostly following the relation $q \approx 23\,M_\odot/M_{\rm ZAMS,1}$ with $M_{\rm ZAMS,1} \gtrsim 250\,{\rm M}_\odot$ and large initial separations $a \gtrsim 10^3\,{\rm M}_\odot$. Such systems evolve through channel III triggering a Roche-lobe overflow episode that becomes unstable when the primary star enters the red super-giant phase. Systems with smaller initial separation merge due to a double Roche-lobe overflow. Only systems with initial $q_{\rm ZAMS} < 0.15$ can evolve through this channel. This is the reason why most of the high-mass primaries come from the model LOG3, followed by LOG4 and LOG1, LOG2 (see Figs. 3, 4 and 5). The fact we do not see this feature in the model LOG3 of Pop. II stars is related to the evolution of radius. High-mass Pop II stars reach the radius to start the interaction earlier than Pop. III stars (see Fig. 2).

4.3 Comparison with previous work

Several authors have explored the formation of BBHs from Pop. III stars (e.g., Kinugawa et al. 2014, 2016, 2020; Hartwig et al. 2016; Belczynski et al. 2017; Liu & Bromm 2020b; Tanikawa et al. 2021b, 2022a,b; Wang et al. 2022). The ZAMS mass range we consider in this work is comparable to the one explored by Tanikawa et al. (2021b). In our models, we do not have any mergers with both BHs above the mass gap, while these are very common in their fiducial model. This discrepancy stems from the intrinsic differences between our single star evolution models. In fact, the very massive stars ($M_{\rm ZAMS} > 200\,{\rm M}_\odot$) considered by Tanikawa et al. (2021b) end the

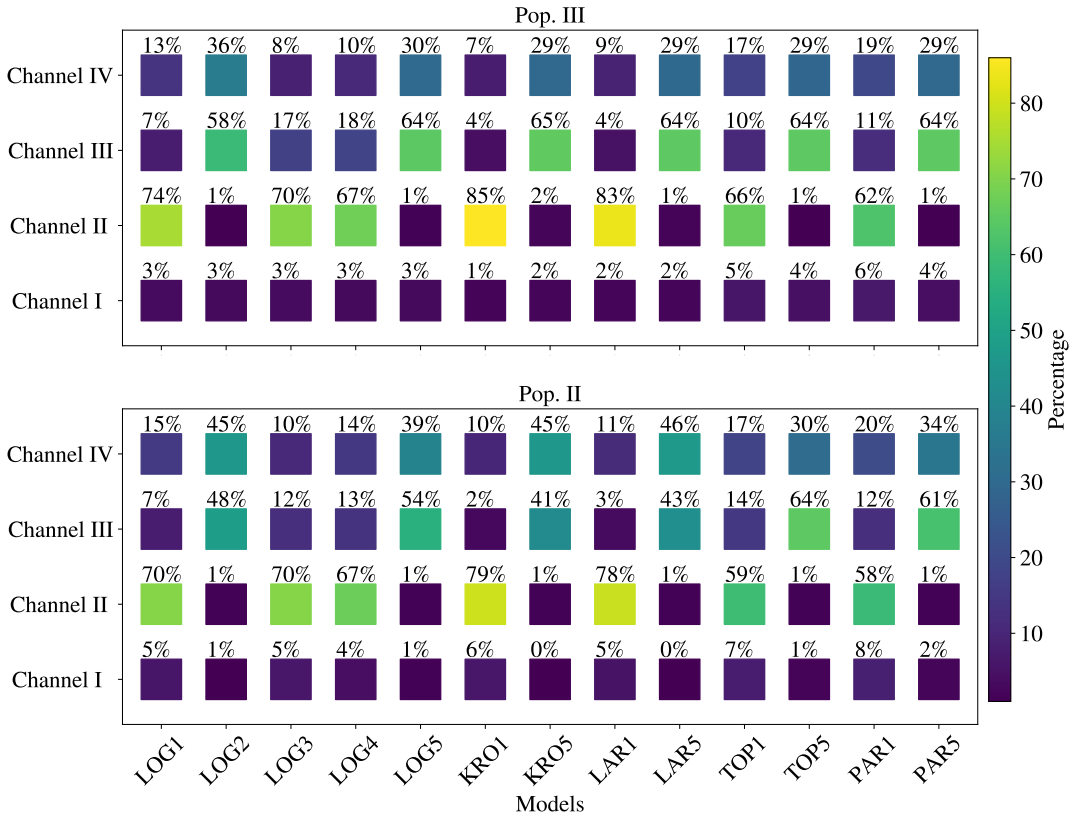

Figure 13. Percentage of BBH mergers that evolve via each of the four channels considered in this work. The x-axis refers to the simulation set, while the y-axis specifies the channel. The upper (lower) panel refers to BBHs that form from Pop. III (II) stars.

MS as compact blue super-giant stars, while our very massive stars expand during the MS and become red super-giant stars already at the end of the MS. As a consequence, the very massive binary systems by Tanikawa et al. (2021b) undergo stable mass transfer and leave BHs above the mass gap, while our very massive binary systems start an unstable common envelope phase as soon as they leave the MS and merge prematurely, before becoming BHs.

The same line of reasoning explains why our delay times (Figs. 12 and Figs. 17) are generally much shorter than the one presented, e.g., in Figure 3 from Tanikawa et al. (2021a). Almost all BBH mergers from Pop. III stars evolve via stable mass transfer in the models by Tanikawa et al. (2021a) and thus have long delay times, while our channel IV mergers (which do not form in Tanikawa et al. 2021a) have very short delay times. These results confirm the key role of single star evolution (including uncertainties about core overshooting, convection and rotation) for the formation of merging BBHs.

5 SUMMARY AND CONCLUSIONS

We have presented a new set of Pop. III stars ($Z = 10^{-11}$) obtained with the stellar evolution code PARSEC (Bressan et al. 2012; Costa et al. 2019, 2021). Our Pop. III stars range from 2 to 600 $M_\odot$. With respect to Pop. II stars ($Z = 10^{-4}$), Pop. III stars with initial mass $M_{\rm ZAMS} \in [14, 40]$ $M_\odot$ evolve with much more compact radii ($R \ll 10^2$ $R_\odot$). Furthermore, the most massive Pop. III stars ($M_{\rm ZAMS} >$ 100 $M_\odot$) end their lives as blue super-giant stars, whereas Pop. II stars in the same mass range die as yellow and red super-giant stars.

We use these tracks as input tables for our fast binary population synthesis code SEVN (Spera et al. 2019; Mapelli et al. 2020; Iorio et al. 2023), in order to study the population of BHs and BBHs born from Pop. II and Pop. III stars. We explore a variety of initial conditions for our binary stars, including a flat-in-log, a Kroupa (K01), a Larson (L98), a top-heavy, and a Park (P23) IMF.

We estimate similar BH masses from the evolution of single massive Pop. II and Pop. III stars. In our fiducial model, the maximum BH mass below the pair-instability gap is 91 and 86 $M_\odot$ for Pop. II and III stars, respectively. Above the gap, both Pop. II and Pop. III stars produce BHs more massive than ≈ 230 $M_\odot$ if they can achieve a ZAMS mass of $\gtrsim 240$ $M_\odot$ (Figure 6). Assumptions on core overshooting, envelope undershooting, and stellar rotation can significantly affect this result, because they influence the mass of the He and CO cores, hence the central temperature and density. Furthermore, these results stem from the assumption that the residual H-rich envelope is not ejected during the failed supernova (e.g., Costa et al. 2022).

Most BBH mergers from both Pop. II and Pop. III stars have primary BH mass below the mass gap. In order to populate the region above the gap, we need very compact stellar radii, that can be achieved either with fast rotation (chemically homogeneous evolution, de Mink & Belczynski 2015) or by suppressing core overshooting (Tanikawa et al. 2022b). With our evolutionary models, we find no mergers with secondary BH mass above the gap. We expect that only dynamics of dense stellar systems can pair up BHs with both primary and secondary mass above the gap, and populate the gap as well (e.g., Mapelli et al. 2022; Wang et al. 2022).

The mass ratios are one of the main signatures of Pop. III versus Pop. II BBHs. In most of our models, Pop. II BBHs are predominantly equal-mass systems, whereas Pop. III BBHs have a peak at

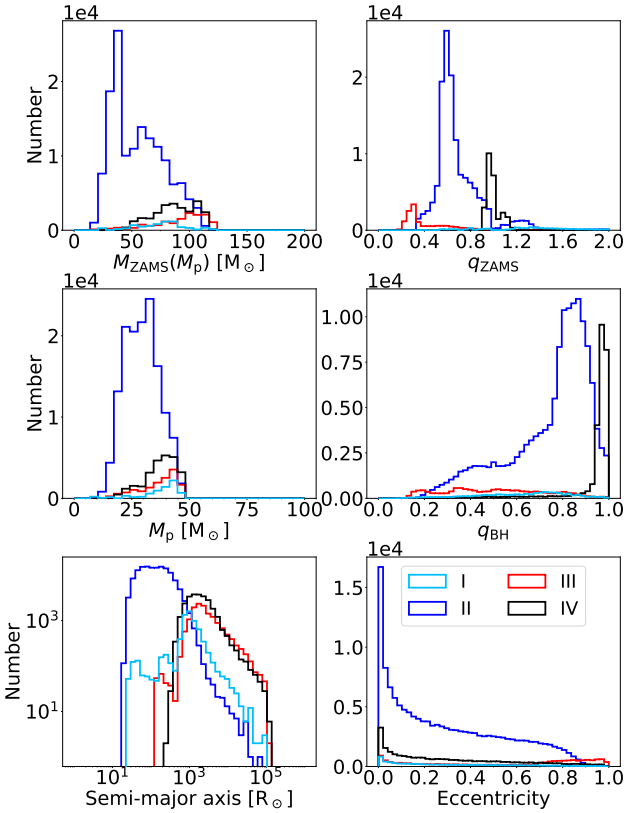

Figure 14. Main properties of BBH mergers and their progenitors in model LOG1 for Pop. III stars. From top to bottom and from left to right: ZAMS mass of the progenitor of the primary BH $M_{\rm ZAMS}(M_{\rm p})$, mass ratio of the progenitors $q_{\rm ZAMS} = M_{\rm ZAMS}(M_{\rm s})/M_{\rm ZAMS}(M_{\rm p})$ (i.e. the ratio between the ZAMS mass of the progenitor of the secondary BH and the ZAMS mass of the progenitor of the primary BH), mass of the primary BH ($M_{\rm p}$), mass ratio of the two BHs ($q_{\rm BH} = M_{\rm s}/M_{\rm p}$), initial semi-major axis (a), initial eccentricity (e). Light-blue line: channel I, blue line: channel II, red line: channel III, black line: channel IV.

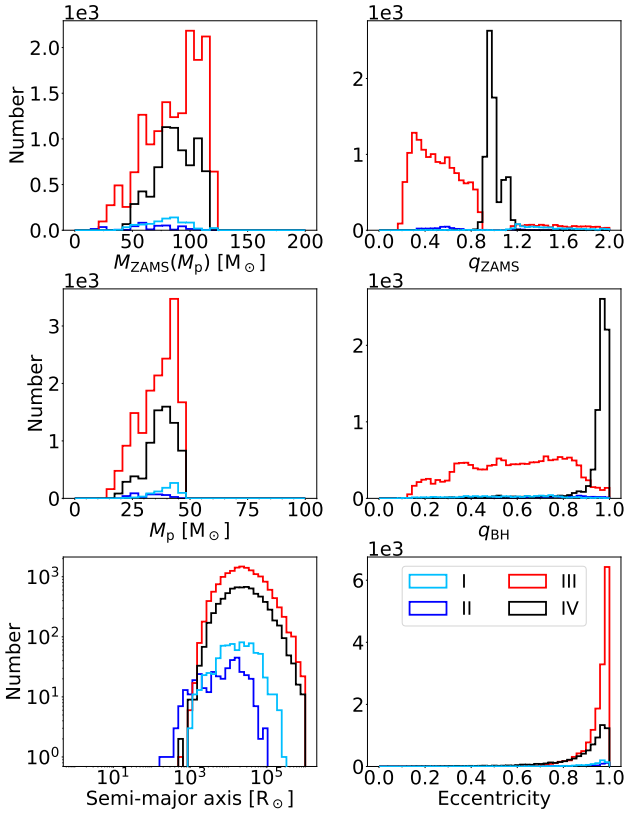

Figure 15. Same as Figure 14 but for model LOG5 for Pop. III stars.

mass ratio $q_{\rm BH} = 0.8 - 0.9$. This difference is too subtle for current detectors, even at a population level, but it can be investigated with next-generation ground-based detectors.

A distinctive signature of Pop. III and II BBHs with respect to BBHs born from metal-rich stars are the evolutionary channels. Assuming the orbital period distribution from Sana et al. (2012), the vast majority (60−80%) of Pop. III and II progenitor stars of BBH mergers evolve via channel II, i.e. just stable mass transfer, with no common envelope. In contrast, at higher metallicity ($Z \sim 2\times10^{-3} - 10^{-2}$) and with the same set-up for binary evolution, the dominant evolutionary pathway (50 − 80% BBH mergers) becomes channel I, characterized by a common envelope between the first-born BH and its companion star (Iorio et al. 2023).

If we instead assume that Pop. III binary systems have longer orbital periods (e.g., Stacy & Bromm 2013), both channels I and II are suppressed: most Pop. III and Pop. II BBHs form from an early common-envelope episode that involves the two progenitor stars, before the formation of the first-born BH (channels III and IV).

Overall, our models show that Pop. III and II stars produce a similar BBH population, especially if we adopt the same IMF and initial orbital properties. The actual IMF and maximum mass of metal-poor and metal-free stars are two of the main sources of uncertainty.

ACKNOWLEDGEMENTS

We are grateful to Simon Glover, Tilman Hartwig, Tomoya Kinugawa, Mario Spera, and Ataru Tanikawa for their enlightening comments. GC, GI, MM, and FS acknowledge financial support from the European Research Council for the ERC Consolidator grant DEMOBLACK, under contract no. 770017. MM and RSK acknowledge financial support from the German Excellence Strategy via the Heidelberg Cluster of Excellence (EXC 2181 - 390900948) "STRUCTURES". This research made use of NumPy (Harris et al. 2020), SciPy (Virtanen et al. 2020), IPython (Perez & Granger 2007). For the plots we used Matplotlib (Hunter 2007).

DATA AVAILABILITY

The data underlying this article and the SEVN configurations files are available on Zenodo at `https://doi.org/10.5281/zenodo.7736309` (Costa et al. 2023). SEVN is publicly available at `https://gitlab.com/sevncodes/sevn.git`: the version used in this work is the commit `0f9ae3bf` in the branch `Costa23popIII` (`https://gitlab.com/sevncodes/sevn/-/tree/Costa23popIII`). Further data will be shared on reasonable request to the corresponding authors.

REFERENCES

Abbott B. P., et al., 2019, ApJ, 882, L24
Abbott R., et al., 2020a, Phys. Rev. Lett., 125, 101102
Abbott R., et al., 2020b, ApJ, 900, L13

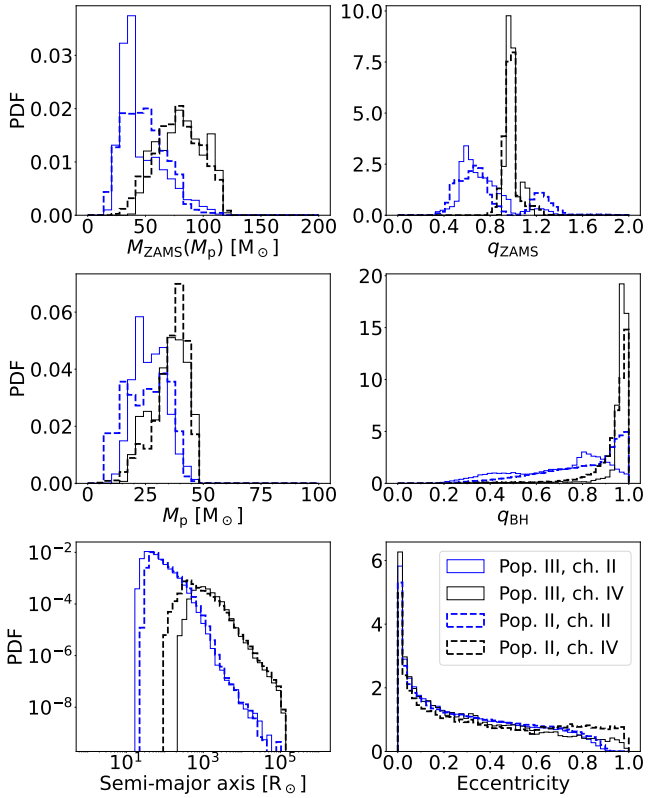

Figure 16. Same as Figure 14 but here we show the KRO1 model and compare BBHs from Pop. III (solid lines) and Pop. II stars (dashed lines). We show only channel II and IV because they are the two most important channels (especially channel II, Fig. 13) and to make the plot more readable.

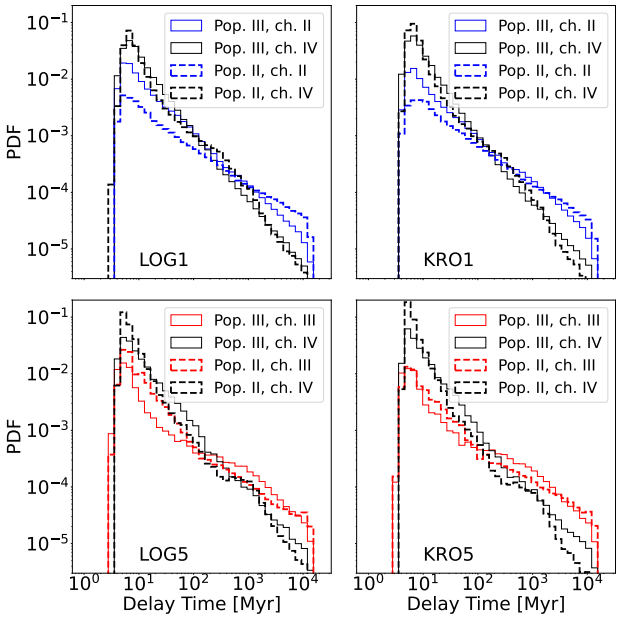

Figure 17. Delay time distribution for Pop. II and Pop. III BBHs (dashed thick and solid thin lines, respectively). From left to right and from top to bottom: models LOG1, KRO1, LOG5 and KRO5. In each panel, we show only the two most important channels for each considered model: channels II and IV in the upper panels, and channels III and IV in the lower panels.

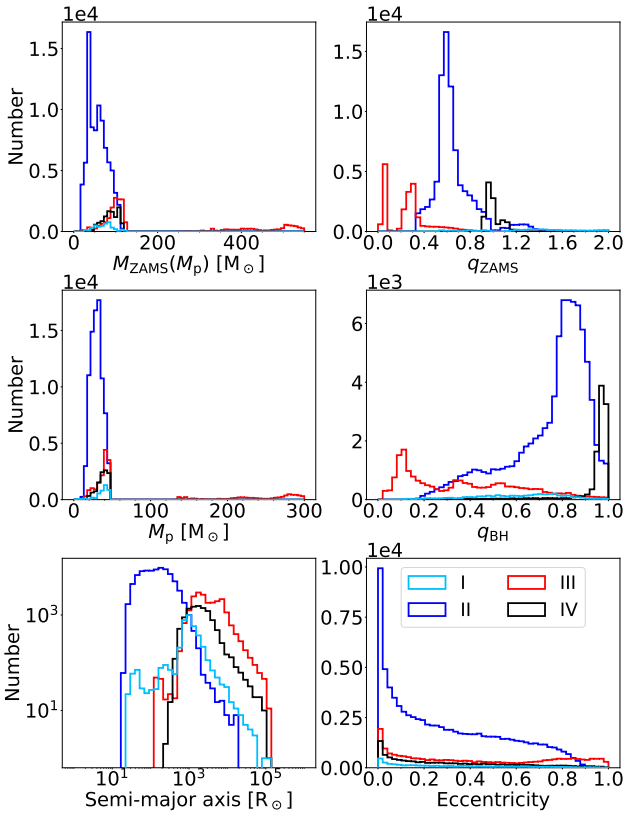

Figure 18. Same as Fig. 14 but for model LOG3 for Pop. III stars.

Abbott R., et al., 2021a, arXiv e-prints, p. arXiv:2108.01045
Abbott R., et al., 2021b, arXiv e-prints, p. arXiv:2111.03606
Abbott R., et al., 2021c, ApJ, 913, L7
Abbott R., et al., 2023, Physical Review X, 13, 011048
Abel T., Bryan G. L., Norman M. L., 2002, Science, 295, 93
Agrawal P., Hurley J., Stevenson S., Rodriguez C. L., Szécsi D., Kemp A., 2023, MNRAS, 525, 933
Barkat Z., Rakavy G., Sack N., 1967, Phys. Rev. Lett., 18, 379
Belczynski K., Ryu T., Perna R., Berti E., Tanaka T. L., Bulik T., 2017, MNRAS, 471, 4702
Böhm-Vitense E., 1958, Z. Astrophys., 46, 108
Bray J. C., Eldridge J. J., 2016, MNRAS, 461, 3747
Bray J. C., Eldridge J. J., 2018, MNRAS, 480, 5657
Bressan A. G., Chiosi C., Bertelli G., 1981, A&A, 102, 25
Bressan A., Marigo P., Girardi L., Salasnich B., Dal Cero C., Rubele S., Nanni A., 2012, MNRAS, 427, 127
Bromm V., 2013, Reports on Progress in Physics, 76, 112901
Bromm V., Larson R. B., 2004, ARA&A, 42, 79
Caffau E., Ludwig H. G., Steffen M., Freytag B., Bonifacio P., 2011, Sol. Phys., 268, 255
Cassisi S., Castellani V., 1993, ApJS, 88, 509
Chen Y., Bressan A., Girardi L., Marigo P., Kong X., Lanza A., 2015, MNRAS, 452, 1068
Chiaki G., Susa H., Hirano S., 2018, MNRAS, 475, 4378
Chiosi C., Bressan A., Portinari L., Tantalo R., 1998, A&A, 339, 355
Chon S., Omukai K., Schneider R., 2021, MNRAS, 508, 4175
Claeys J. S. W., Pols O. R., Izzard R. G., Vink J., Verbunt F. W. M., 2014, A&A, 563, A83
Costa G., Girardi L., Bressan A., Marigo P., Rodrigues T. S., Chen Y., Lanza A., Goudfrooij P., 2019, MNRAS, 485, 4641

Costa G., Bressan A., Mapelli M., Marigo P., Iorio G., Spera M., 2021, MNRAS, 501, 4514
Costa G., Ballone A., Mapelli M., Bressan A., 2022, MNRAS, 516, 1072
Costa G., Mapelli M., Iorio G., Santoliquido F., Escobar G. J., Bressan A., 2023, Data from "Massive binary black holes from Population II and III stars", doi:10.5281/zenodo.7736309, https://doi.org/10.5281/zenodo.7736309
Dominik M., Belczynski K., Fryer C., Holz D. E., Berti E., Bulik T., Mandel I., O'Shaughnessy R., 2012, ApJ, 759, 52
Farmer R., Renzo M., de Mink S. E., Marchant P., Justham S., 2019, ApJ, 887, 53
Farmer R., Renzo M., de Mink S. E., Fishbach M., Justham S., 2020, ApJ, 902, L36
Fernández R., Quataert E., Kashiyama K., Coughlin E. R., 2018, MNRAS, 476, 2366
Fowler W. A., Hoyle F., 1964, ApJS, 9, 201
Frebel A., Norris J. E., 2015, ARA&A, 53, 631
Frebel A., Johnson J. L., Bromm V., 2007, MNRAS, 380, L40
Fryer C. L., Belczynski K., Wiktorowicz G., Dominik M., Kalogera V., Holz D. E., 2012, ApJ, 749, 91
Giacobbo N., Mapelli M., 2019, MNRAS, 482, 2234
Giacobbo N., Mapelli M., 2020, ApJ, 891, 141
Glover S., 2013, in Wiklind T., Mobasher B., Bromm V., eds, Astrophysics and Space Science Library Vol. 396, The First Galaxies. p. 103, doi:10.1007/978-3-642-32362-1_3
Goswami S., et al., 2022, A&A, 663, A1
Harris C. R., et al., 2020, Nature, 585, 357
Hartwig T., Volonteri M., Bromm V., Klessen R. S., Barausse E., Magg M., Stacy A., 2016, MNRAS, 460, L74
Herwig F., Bloecker T., Schoenberner D., El Eid M., 1997, A&A, 324, L81
Hirano S., Hosokawa T., Yoshida N., Umeda H., Omukai K., Chiaki G., Yorke H. W., 2014, ApJ, 781, 60
Hirano S., Hosokawa T., Yoshida N., Omukai K., Yorke H. W., 2015, MNRAS, 448, 568
Hobbs G., Lorimer D. R., Lyne A. G., Kramer M., 2005, MNRAS, 360, 974
Hunter J. D., 2007, Computing in Science & Engineering, 9, 90
Hurley J. R., Tout C. A., Pols O. R., 2002, MNRAS, 329, 897
Iorio G., et al., 2023, MNRAS, 524, 426
Jaacks J., Finkelstein S. L., Bromm V., 2019, MNRAS, 488, 2202
Jaura O., Glover S. C. O., Wollenberg K. M. J., Klessen R. S., Geen S., Haemmerlé L., 2022, MNRAS, 512, 116
Kinugawa T., Inayoshi K., Hotokezaka K., Nakauchi D., Nakamura T., 2014, MNRAS, 442, 2963
Kinugawa T., Miyamoto A., Kanda N., Nakamura T., 2016, MNRAS, 456, 1093
Kinugawa T., Nakamura T., Nakano H., 2020, MNRAS, 498, 3946
Klessen R. S., Glover S. C. O., 2023, arXiv e-prints, p. arXiv:2303.12500
Kroupa P., 2001, MNRAS, 322, 231
Kruckow M. U., Tauris T. M., Langer N., Kramer M., Izzard R. G., 2018, MNRAS, 481, 1908
Larson R. B., 1998, MNRAS, 301, 569
Leung S.-C., Nomoto K., Blinnikov S., 2019, ApJ, 887, 72
Liu B., Bromm V., 2020a, MNRAS, 495, 2475
Liu B., Bromm V., 2020b, ApJ, 903, L40
Mapelli M., Spera M., Montanari E., Limongi M., Chieffi A., Giacobbo N., Bressan A., Bouffanais Y., 2020, ApJ, 888, 76
Mapelli M., Bouffanais Y., Santoliquido F., Arca Sedda M., Artale M. C., 2022, MNRAS, 511, 5797
Marchant P., Renzo M., Farmer R., Pappas K. M. W., Taam R. E., de Mink S. E., Kalogera V., 2019, ApJ, 882, 36
Marchant P., Pappas K. M. W., Gallegos-Garcia M., Berry C. P. L., Taam R. E., Kalogera V., Podsiadlowski P., 2021, A&A, 650, A107
Marigo P., Girardi L., Chiosi C., Wood P. R., 2001, A&A, 371, 152
Murphy L. J., et al., 2021, MNRAS, 501, 2745
Nguyen C. T., et al., 2022, A&A, 665, A126
Park J., Ricotti M., Sugimura K., 2021a, MNRAS, 508, 6176
Park J., Ricotti M., Sugimura K., 2021b, MNRAS, 508, 6193
Park J., Ricotti M., Sugimura K., 2023, MNRAS, 521, 5334
Perez F., Granger B. E., 2007, Computing in Science Engineering, 9, 21
Prole L. R., Clark P. C., Klessen R. S., Glover S. C. O., 2022, MNRAS, 510, 4019
Rakavy G., Shaviv G., 1967, ApJ, 148, 803
Renzo M., Farmer R., Justham S., Götberg Y., de Mink S. E., Zapartas E., Marchant P., Smith N., 2020a, A&A, 640, A56
Renzo M., Cantiello M., Metzger B. D., Jiang Y. F., 2020b, ApJ, 904, L13
Sana H., et al., 2012, Science, 337, 444
Santoliquido F., Mapelli M., Iorio G., Costa G., Glover S. C. O., Hartwig T., Klessen R. S., Merli L., 2023, MNRAS,
Schneider R., Omukai K., Inoue A. K., Ferrara A., 2006, MNRAS, 369, 1437
Schneider R., Omukai K., Bianchi S., Valiante R., 2012, MNRAS, 419, 1566
Schwarzschild M., 1958, Structure and evolution of the stars.. Princeton, Princeton University Press, 1958.
Sharda P., Krumholz M. R., 2022, MNRAS, 509, 1959
Smith B. D., Wise J. H., O'Shea B. W., Norman M. L., Khochfar S., 2015, MNRAS, 452, 2822
Spera M., Mapelli M., 2017, MNRAS, 470, 4739
Spera M., Mapelli M., Giacobbo N., Trani A. A., Bressan A., Costa G., 2019, MNRAS, 485, 889
Stacy A., Bromm V., 2013, MNRAS, 433, 1094
Stevenson S., Sampson M., Powell J., Vigna-Gómez A., Neijssel C. J., Szécsi D., Mandel I., 2019, ApJ, 882, 121
Sugimura K., Matsumoto T., Hosokawa T., Hirano S., Omukai K., 2020, ApJ, 892, L14
Susa H., Hasegawa K., Tominaga N., 2014, ApJ, 792, 32
Tanikawa A., Kinugawa T., Yoshida T., Hijikawa K., Umeda H., 2021a, MNRAS, 505, 2170
Tanikawa A., Susa H., Yoshida T., Trani A. A., Kinugawa T., 2021b, ApJ, 910, 30
Tanikawa A., Chiaki G., Kinugawa T., Suwa Y., Tominaga N., 2022a, PASJ, 74, 521
Tanikawa A., Yoshida T., Kinugawa T., Trani A. A., Hosokawa T., Susa H., Omukai K., 2022b, ApJ, 926, 83
Valiante R., Schneider R., Volonteri M., Omukai K., 2016, MNRAS, 457, 3356
Vink J. S., Higgins E. R., Sander A. A. C., Sabhahit G. N., 2021, MNRAS, 504, 146
Virtanen P., et al., 2020, Nature Methods, 17, 261
Volpato G., Marigo P., Costa G., Bressan A., Trabucchi M., Girardi L., 2023, ApJ, 944, 40
Wang L., Tanikawa A., Fujii M., 2022, MNRAS, 515, 5106
Wollenberg K. M. J., Glover S. C. O., Clark P. C., Klessen R. S., 2020, MNRAS, 494, 1871
Woosley S. E., 2017, ApJ, 836, 244
Woosley S. E., 2019, ApJ, 878, 49
Woosley S. E., Heger A., 2021, ApJ, 912, L31
Woosley S. E., Heger A., Weaver T. A., 2002, Reviews of Modern Physics, 74, 1015
Woosley S. E., Blinnikov S., Heger A., 2007, Nature, 450, 390
Yoshida N., Omukai K., Hernquist L., Abel T., 2006, ApJ, 652, 6
de Mink S. E., Belczynski K., 2015, ApJ, 814, 58